HIGH-FIDELITY MODELING AND CONTROL SYSTEM SYNTHESIS FOR A DRAG-FREE MICROSATELLITE

Sumeet Singh, Simone D'Amico, and Marco Pavone
Department of Aeronautics and Astronautics, Stanford University, Stanford CA 94305
{ssingh19, damicos, pavone}@stanford.edu

Abstract: *A drag-free satellite is a spacecaft composed of an internal test mass shielded by an external satellite that compensates all dominant disturbance forces encountered in the space environment such as aerodynamic drag and solar radiation pressure. By minimizing all non-gravitational disturbances on the test mass, the trajectory of the spacecraft is a near perfect geodesic. In concert with precise orbit determination techniques, drag-free satellites allow us to investigate topics in geodesy, aeronomy, and gravitational physics and conduct challenging experiments in low-disturbance environments to unprecedented accuracy. This paper addresses the development of a high-fidelity simulator and control system design for the Modular Gravitational Reference Sensor (MGRS) drag-free satellite. MGRS is a 100 kg microsatellite due to launch in 2018 into a Sun-synchronous orbit with a mean altitude of 657 km that aims to demonstrate three-axis drag-free operations with residual non-gravitational acceleration of a test mass under* $10^{-12} ms^{-2}/\sqrt{Hz}$ *in the frequency range 0.01 to 1 Hz. The drag-free performance goal reflects a substantial improvement upon past drag-free missions such as TRIAD I, GPB, and GOCE, and will be accomplished at a fraction of the cost. Additionally, this mission represents a key technology demonstration within a larger research endeavour that aims to develop a multi-purpose distributed drag-free architecture based on microsatellite platforms. Our modeling framework allows us to gain a comprehensive insight into the range of expected disturbances, derive sizing constraints for a suitable micropropulsion system, and formulate a preliminary drag-free translational and attitude control system using* $H_\infty-$ *control techniques.*

Keywords: *Drag-free satellite, satellite simulation, drag-free control,* $H_\infty-$ *control.*

1. Introduction

Since the introduction of drag-free satellites in [1], they have served as promising platforms for facilitating precise experimental physics in areas such as geodesy, remote sensing and relativistic science [2, 3, 4, 5]. The first drag-free satellite Triad I [6] was flown in 1972 and achieved a proof mass residual acceleration of $5 \cdot 10^{-11}$ ms^{-2} (RMS) averaged over three days. Since then there have been two more drag-free missions: Gravity Probe B (GPB) [7], and the Gravity Field and Steady-State Ocean Circulation Explorer (GOCE) [8]. The GPB experiment was an attempt to validate two predictions of General Relativity: the geodetic and frame-dragging effects. The mission achieved residual inertial accelerations for the test mass gyroscope under $4 \cdot 10^{-11}$ ms^{-2} along the roll axis and less than $2 \cdot 10^{-10}$ ms^{-2} in the tranverse axes, averaged between 0.01-10 mHz [9]. GOCE studied the Earth's gravitational field to unprecedented spatial resolution and accuracy and yielded a new global model for the Earth's geoid. The drag-free controller achieved a residual linear acceleration noise floor in the along-track direction under 10^{-9} ms$^{-2}/\sqrt{\text{Hz}}$ between 5 mHz - 0.1 Hz [8]. The next generation of drag-free missions conducting ultra-precise relativistic experiments face even more stringent requirements on the drag-free performance.

LISA Pathfinder (LPF) [10] is a joint ESA/NASA mission that will test critical technologies for the proposed Laser Interferometric Space Antenna (LISA) gravitational wave detection mission [11]. Among other objectives, LPF's drag-free goal is to constrain the relative acceleration noise between a pair of cubic test masses to be below:

$$3 \cdot 10^{-14} \left[1 + \left(\frac{f}{3\text{mHz}} \right)^2 \right] \text{ms}^{-2}/\sqrt{\text{Hz}},$$

over the frequency range $1 - 30$ mHz. The CNES mission Microscope [12] will attempt to measure the

weak equivalence principle to an accuracy of 10^{-15} and will require drag-free control with residual non-gravitational acceleration below 10^{-12} ms$^{-2}/\sqrt{\text{Hz}}$ within the same frequency range.

The Modular Gravitational Reference Sensor (MGRS) satellite is a drag-free technology demonstration mission planned for launch in 2018 with three main objectives: (a) validate the performance of the Differential Optical Shadow Sensor (DOSS) as a gravitational reference sensor [13, 14], (b) demonstrate three-axis drag-free operation with residual acceleration of the test mass under 10^{-12} ms$^{-2}/\sqrt{\text{Hz}}$ within the science frequency band $\mathcal{B} := [0.01, 1]$ Hz, and (c) demonstrate Precise Orbit and Gravity Determination (POGD) capability at the centimeter level using multi-constellation Global Navigation Satellite System (GNSS) receivers [15, 16]. MGRS will be the second of a series of missions planned by the newly formed Center of Excellence in Aeronautics and Astronautics (CEAA), a joint partnership between Stanford University, King Abdulaziz City for Science and Technology (KACST), and NASA Ames. The first mission in this series, UVLED, was launched in June 2014 and validated the use of UV LEDs for charge control of a test mass. Missions beyond MGRS will test novel technological developments in areas such as precision timekeeping, non-cooperative rendezvous, and cooperative drag-free formation flight, to conduct challenging experiments in geodetic and relativistic science [17].

In addition to the drag-free performance objective, MGRS exemplifies the increasing proclivity towards the use of smaller spacecraft such as nanosatellites (< 10 kg) and microsatellites (< 100 kg) in efforts to reduce cost and development time [18, 19]. Among the several challenges that such a trend introduces (e.g. miniaturization of power subsystems and scientific payloads), the key parameter of interest for drag-free missions is actuation, i.e. micropropulsion. The ability to achieve an extremely low disturbance environment for the test mass is strongly reliant on the performance abilities of a high precision micropropulsion system. The need for such small thrusts stems from: (a) a low disturbance environment in space, and (b) miniscule required corrections to the external satellite (on the order of μm) to maintain adequate separation between the external satellite and the test mass. GPB had the advantage of having access to a large amount of Helium gas for the on-board experiment. Consequently, the drag-free control system was able to use this gas as propellant within a proportional control scheme [20]. GOCE, on account of its low orbit altitude of 235 km experienced in-track forces large enough to be easily compensated by a 20 mN Kaufman-type ion thruster. The lateral force and torque compensation however posed some difficulty due to lack of maturity in electric propulsion technology at such low thrust levels [21].

MGRS is a 100 kg microsatellite modeled on the SaudiSat 4 satellite bus (see Figure 2). It consists of a rectangular cuboid body with dimensions $670 \times 572 \times 550$ mm with four depolyable solar panels. The satellite houses a free-floating 2.5 cm spherical BeCu test mass whose position with respect to the satellite is measured by the DOSS assembly. Due to the satellite's small size, the expected non-conservative disturbance forces in Low Earth Orbit (LEO) are quite small. Indeed, at an altitude of 657 km, the radial disturbance forces are estimated to be less than 1 μN. The lack of space to accomodate large quantities of propellant (e.g. for a cold-gas micropropulsion system [22]) and limited power budget (< 160 W for the entire satellite) make the selection of a suitable micropropulsion system quite challenging. In this paper we discuss the development of a drag-free and attitude control system for MGRS that leverages existing technology, thereby establishing the possibility of achieving extremely precise drag-free performance on a tightly constrained platform.

In order to synthesize an appropriate control system for MGRS, it is essential to first obtain a detailed characterization of all forces and torques on the satellite and test mass. This not only includes external non-conservative forces such as aerodynamic drag, solar and Earth radiation pressure, but also the interactions between the satellite and the test mass itself such as electromagnetic and self-gravity gradients. Consequently, the contributions of this paper are as follows: first, we detail the modeling assumptions and development of a high-fidelity simulation environment that provides insights into the range of expected disturbances (both external and internal) for a near circular Sun-synchronous orbit at a mean altitude of 657

km. Second, the disturbance simulation results are used to select a suitable micropropulsion system based on a trade-study involving several options such as ion-engines, cold-gas and electrospray thrusters. Suitability here is defined by two key characteristics: (a) satisfaction of the power, mass and volume constraints, and (b) precision thrust controllability and sub-μN level noise. Third, we formalize the drag-free performance objective and propulsion constraints within a translational and attitude control system framework. In particular, we illustrate the nonlinear coupling between the translational and rotational dynamics induced by the drag-free performance bounds, highlight fundamental limitations for control, and present a method for decoupling the control design. Finally, we employ $H_\infty-$optimization based techniques to synthesise the drag-free and attitude controllers and implement them within the high-fidelity simulator. Our results demonstrate that the residual acceleration of the test mass is below the target bound of 10^{-12} $\text{ms}^{-2}/\sqrt{\text{Hz}}$ with margin using existing micropropulsion technology, thereby establishing microsatellites as feasible platforms for hosting precise experiments in space.

The rest of the paper is organized as follows: Section 2. introduces the notation that is used for the rest of the paper; Sections 3., 4. and 5. detail the time and reference frame conventions, equations of motion, and force and torque modeling for the high fidelity simulator, concluding with simulation results. In Section 6., we present our discussion on the selection of a micropropulsion system, formalize the drag-free and attitude control problems, and formulate controllers using $H_\infty-$optimization. Section 7. validates the controllers synthesized in Section 6. by implementing them within the full nonlinear simulation environment. Finally, we present our conclusions in Section 8. with a discussion on future work that will explicitly account for model uncertainties and utilize online disturbance estimation techniques within a robust, adaptive control framework.

2. Notation

For vectors $\boldsymbol{a}, \boldsymbol{b} \in \mathbb{R}^3$, the dot and cross products are denoted as $\boldsymbol{a} \cdot \boldsymbol{b}$ and $\boldsymbol{a} \times \boldsymbol{b}$ respectively. Unit vectors are denoted by an overhead $(\hat{\cdot})$, i.e. $\hat{\boldsymbol{a}} := \boldsymbol{a}/\|\boldsymbol{a}\|_2$ where $\|\cdot\|_2$ denotes the usual Euclidean norm. Let I_n denote an $n \times n$ identity matrix. Given (possibly Multiple Input Multiple Output) transfer functions w_1, w_2 and w_3, we define $\text{diag}(w_1, w_2, w_3)$ to denote a block diagonal matrix where the blocks are the individual transfer functions. The singular values of a Multiple Input Multiple Output (MIMO) system w are denoted by $\sigma(w)$, and the maximum and minimum singular values are defined as $\bar{\sigma}(w)$ and $\underline{\sigma}(w)$ respectively. For a vector $\boldsymbol{b} = [b_1, b_2, b_3]^T$, its skew-symmetric form Ω is defined as as:

$$\Omega := \begin{bmatrix} 0 & -b_3 & b_2 \\ b_3 & 0 & -b_1 \\ -b_2 & b_1 & 0 \end{bmatrix}.$$

Let $\widetilde{q}$ denote the amplitude spectral density (ASD) of the variable q. That is, if q has units 'x', $\widetilde{q}$ has units $\text{x}/\sqrt{\text{Hz}}$. Finally, in this paper we will clearly distinguish between vector and matrix equations. In particular, any time-derivatives in vector equations will be referenced to an observer in the inertial or body frame by the subscripts $(\cdot)_I$ and $(\cdot)_B$ respectively. Time-derivatives in matrix equations will always refer to the reference frame in which the vector components are expressed. These reference frames are defined in the next section.

3. Time and Reference Frames

The primary Earth Centered Inertial (ECI) frame used in this paper is the Earth Mean Equator - Mean Equinox Dynamical System of J2000 (EME2000). This frame coincides with the Geocentric Celestial Reference Frame (GCRF) to within tens of milli-arcseconds [23]. The Earth Centered Earth Fixed (ECEF) frame is the International Terrestial Reference Frame (ITRF).

Transformation between the ECI and ECEF frames is done using the IAU-76/FK5 reduction utilizing the IAU-76 Precession, IAU-80 Theory of Nutation, and IAU-82 Sidereal time models. The algorithm imple-

mented is outlined in [23]. For a position vector $\boldsymbol{r}_I$ in the ECI frame, the equivalent position in the ECEF frame $\boldsymbol{r}_E$, is given by:

$$\boldsymbol{r}_E = \Pi(t)\Theta(t)N(t)P(t)\boldsymbol{r}_I, \tag{1}$$

where $\Pi(t)$, $\Theta(t)$, $N(t)$ and $P(t)$ describe the polar motion, sidereal rotation, nutation[1] and precession transformation matrices respectively. The polar motion coefficients (x_p, y_p), time parameters $\Delta UT1 := UT1 - UTC$, $\Delta AT := TAI - UTC$ and LOD are obtained from the online International Earth Rotation Service (IERS) database.

In addition to the ECI and ECEF frames, the Local Orbital Reference Frame (LORF) is defined in Figure 1.

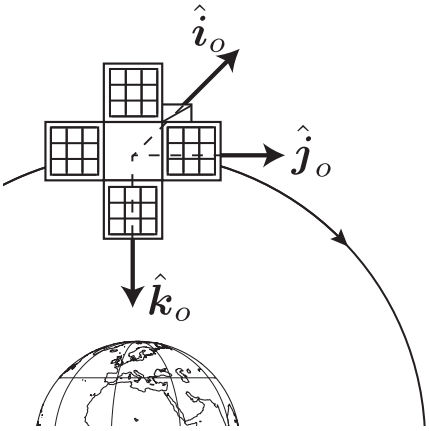

Figure 1: Definition of the Local Orbital Reference Frame with basis vectors: $\hat{\boldsymbol{i}}_o$: Cross-track, $\hat{\boldsymbol{j}}_o$: In-track, $\hat{\boldsymbol{k}}_o$: Zenith (opposite radial).

As MGRS will serve as a stepping stone towards both Earth science and relativistic missions, we forsee various attitude modes during drag-free operations such as inertially fixed or aligned with the LORF and thus possessing a nominal spin equal to the satellite's mean motion around the Earth. In this paper, we study the second mode. The inertially fixed mode can be considered as a subset of the LORF mode by setting the nominal spin to zero. The satellite body fixed frame and its alignment with respect to the LORF is shown in Figure 2. Additional drawings of the satellite with dimensions are provided in Appendix 11.1.

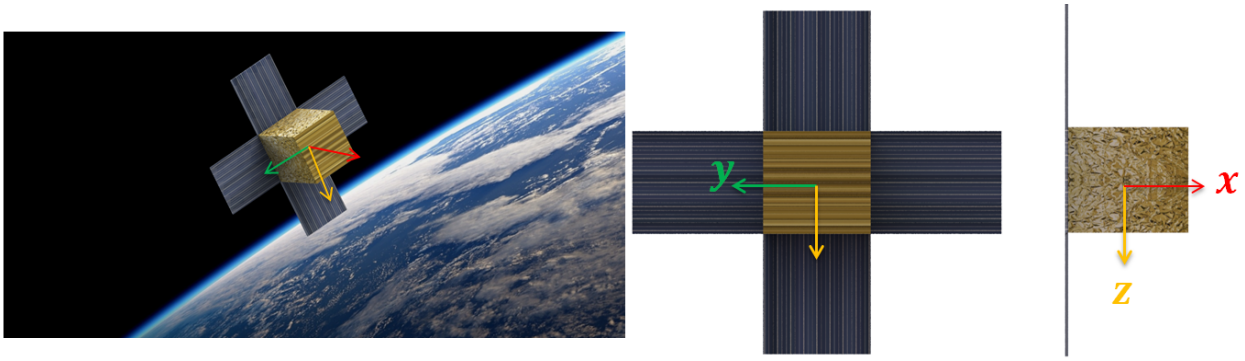

Figure 2: Illustration of the satellite body fixed frame and its aligment with respect to LORF; $x-$axis: Cross-track, $y-$axis: In-track, $z-$axis: Zenith.

As shown in Figure 2, the satellite's $x-$axis is nominally aligned with the cross-track axis of the LORF. Consquently, the satellite possesses a nominal spin about its $x-$axis equal to the mean motion of the satellite around the orbit. To parameterize the satellite attitude with respect to the LORF, we define a set of Euler

[1]Without the extra EOP corrections $\delta\Delta\epsilon_{1980}$ and $\delta\Delta\Psi_{1980}$ as we are not referencing the GCRF frame.

angles: starting from the LORF in Figure 1, we use the rotation order: $z-$axis: Yaw (ψ), $x-$axis: Pitch (θ), $y-$axis: Roll (ϕ).

4. Equations of Motion

Let the ECI position of the satellite center of mass and test mass be given by $\boldsymbol{r}_s$ and $\boldsymbol{r}_p$ respectively. The equations of motion for the test mass and satellite are given by:

$$m_p \ddot{\boldsymbol{r}}_{p_I} = \boldsymbol{F}_{gp} + \boldsymbol{F}_{sp} + \boldsymbol{F}_{dp} \tag{2a}$$

$$m_s \ddot{\boldsymbol{r}}_{s_I} = \boldsymbol{F}_{gs} - \boldsymbol{F}_{sp} + \boldsymbol{F}_{ds} + \boldsymbol{F}_{cs}, \tag{2b}$$

where $\boldsymbol{F}_{gp}$ and $\boldsymbol{F}_{gs}$ are the net *external* (i.e. due to the Earth, Moon, and Sun) gravitational forces on the test mass and satellite respectively; $\boldsymbol{F}_{sp}$ is the disturbance force exerted by the satellite on the test mass hereby denoted as the "stiffness" force; $\boldsymbol{F}_{ds}$ and $\boldsymbol{F}_{dp}$ are direct disturbances on the test mass and satellite respectively, and $\boldsymbol{F}_{cs}$ are the thruster control forces on the satellite. The mass of the satellite and test mass are denoted by m_s (≈ 100 kg) and m_p (≈ 70 g) respectively. For the remainder of the paper, we will refer to the normalized forces (accelerations) by the lowercase $\boldsymbol{f}$ and reserve $\boldsymbol{F}$ to denote actual forces[2] .

The direct forces on the test mass $\boldsymbol{f}_{dp}$ comprise of residual non-gravitational forces not shielded by the external satellite (e.g. collision impacts from cosmic rays, differential pressure forces from satellite component outgassing). As these forces are not dynamically coupled with the satellite, they cannot be mitigated via control and therefore represent a fundamental lower bound on achievable drag-free performance. The stiffness disturbance describes a coupling between the satellite and test mass that can be attributed to several sources such as: magnetic field gradients, self-gravitational forces exerted by the satellite upon the test mass, and electrical stiffness. The magnitudes of the various direct and stiffness disturbances are discussed in detail in [24] for a variety of satellite/test mass configurations. For MGRS, the direct disturbance on the test mass $\boldsymbol{f}_{dp}$ is estimated to have a unilateral ASD less than $4 \cdot 10^{-13}$ $\mathrm{ms}^{-2}/\sqrt{\mathrm{Hz}}$ in all three axes within the MGRS science frequency band $\mathcal{B}$. The stiffness coupling will be discussed in more detail later.

MGRS will be flown in "pure drag-free" mode where the external satellite is flown around the free-floating test mass. This mode of operation differs from the "accelerometer drag-free" mode employed by GPB and GOCE (and proposed for Microscope) where an electrostatic accelerometer is used to control the satellite thrusters to minimize the suspension forces that keep the test mass centered within its housing.

The evolution of the displacement between the satellite and test mass center of mass is described by the relative equation:

$$\ddot{\boldsymbol{r}}_{sp_I} = \ddot{\boldsymbol{r}}_{p_I} - \ddot{\boldsymbol{r}}_{s_I}, \tag{3}$$

where $\boldsymbol{r}_{sp}$ denotes the vector from the satellite center of mass to the test mass. For simulation, the satellite's dynamics are integrated in the ECI frame and the relative satellite/test mass dynamics are integrated in the satellite body frame:

$$\ddot{\boldsymbol{r}}_{sp_B} = \ddot{\boldsymbol{r}}_{sp_I} - \Big(\dot{\boldsymbol{\omega}} \times \boldsymbol{r}_{sp} + 2\boldsymbol{\omega} \times \dot{\boldsymbol{r}}_{sp_B} + \boldsymbol{\omega} \times (\boldsymbol{\omega} \times \boldsymbol{r}_{sp}) \Big), \tag{4}$$

where $\boldsymbol{\omega} := [\omega_x, \omega_y, \omega_z]^T$ is the rotation rate of the satellite body frame with respect to inertial space and $(\cdot)_B$ signifies acceleration and velocity with respect to an observer rotating with the satellite.

The satellite angular velocity $\boldsymbol{\omega}$ and quaternion $\boldsymbol{q}$ with respect to inertial space are governed by the following

[2]The normalization for $\boldsymbol{F}_{sp}$ denoted by $\boldsymbol{f}_{sp}$ is with respect to m_p.

equations:

$$\dot{\boldsymbol{\omega}} = J^{-1}\Big(\boldsymbol{M} - \boldsymbol{\omega} \times I\boldsymbol{\omega}\Big) \tag{5a}$$

$$\dot{\boldsymbol{q}} = \frac{1}{2}\begin{bmatrix}0\\ \boldsymbol{\omega}\end{bmatrix} \odot \boldsymbol{q}, \tag{5b}$$

where $\boldsymbol{M}$ is the sum of the disturbance ($\boldsymbol{M}_d$) and control ($\boldsymbol{M}_c$) torques on the satellite, J is the satellite moment of inertia matrix, and $\odot$ denotes the quaternion product.

We now address the modeling of the various forces and torques on the satellite and test mass with the goal of obtaining an accurate characterization of the expected disturbances, thereby allowing us to formulate the drag-free and attitude control systems.

5. Force and Torque Modeling

This section details the contributions to the various forces and torques in Equations 2a, 2b and 5a for developing the high-fidelity simulator. The models discussed in Sections 5.1.-5.3. can be found in standard spacecraft design literature and the reader may skip directly to Section 5.4. for simulation results without loss in continuity; a short summary for these sections is provided in Table 1.

Modeled Effect	Comments	Relevant terms in 2a 2b and 5a
Gravity	Aspherical harmonic expansion model for Earth Solid Earth tidal effects Third-body effects from the Sun and Moon Gravity gradient disturbance torque	$\boldsymbol{f}_{gs}$, $\boldsymbol{f}_{gp}$, $\boldsymbol{M}_d$
Environmental disturbances	Aerodynamic force and torque Radiation force and torque (Solar and Earth radiation pressure) Magnetic disturbance torque	$\boldsymbol{f}_{ds}$, $\boldsymbol{M}_d$
Stiffness disturbances	Self-gravitational forces (mass-attraction) Electromagnetic forces	$\boldsymbol{f}_{sp}$
Control forces	FEEP thrusters	$\boldsymbol{f}_c$, $\boldsymbol{f}_{ds}$

Table 1: Summary of Modeled effects

Due to the primarily stochastic nature of the direct disturbances on the test mass and the plethora of possible effects (see [24]), the disturbance $\boldsymbol{f}_{dp}$ is modeled as band-limited noise with a unilateral ASD of $4 \cdot 10^{-13}$ $\mathrm{ms}^{-2}/\sqrt{\mathrm{Hz}}$ up to 5 Hz.

5.1. Gravity

5.1.1. Central Body

The aspherical gravitational potential function for the Earth at distance r and geocentric latitude and longitude (ϕ, λ) is given by:

$$U = \frac{\mu_\oplus}{r}\left[1 + \sum_{l=2}^{N_{\max}} \sum_{m=0}^{l} \left(\frac{R_\oplus}{r}\right)^l P_{l,m}(\sin(\phi)) \left[C_{l,m}\cos(m\lambda) + S_{l,m}\sin(m\lambda)\right]\right], \tag{6}$$

where $\mu_\oplus$ is the Earth gravitational potential, $R_\oplus$ is the mean Earth radius, $P_{l,m}$ are the associated Legendre functions, and $C_{l,m}$ and $S_{l,m}$ are the degree l and order m unitless gravitational coefficients. The resulting acceleration given by the gradient of the potential function was obtained by implementing the efficient recursive algorithm derived in [25]. For our simulations we utilized the (tide-free) GRACE GGM001S coefficients upto degree and order 120 (i.e. $N_{\max} = 120$). In addition, we also modeled solid Earth tidal effects using the two step approach outlined in [26] up to degree four.

The gravity gradient torque on the satellite is modeled using a first order binomial expansion for the distance from the Earth center to any given point on the satellite along with the Newtonian two-body gravity model [27]:

$$\boldsymbol{M}_{\text{gg}} = \frac{3\mu_\oplus}{\|\boldsymbol{r}_s\|_2^5}\boldsymbol{r}_s \times I\boldsymbol{r}_s. \tag{7}$$

5.1.2. Third Body

The acceleration of the satellite and test mass (formula given below for satellite) with respect to the Earth due to the Sun and Moon is given by:

$$\sum_{j=1}^{2} \mu_j \left(\frac{\boldsymbol{r}_{sj}}{\|\boldsymbol{r}_{sj}\|_2^3} - \frac{\boldsymbol{r}_j}{\|\boldsymbol{r}_j\|_2^3}\right), \tag{8}$$

where μ_j is the gravitational constant of the third body ($j = 1$: Sun, $j = 2$: Moon), $\boldsymbol{r}_{sj}$ is the vector from the satellite to the third body and $\boldsymbol{r}_j$ is the position of the third body with respect to the Earth.

The positions of the Moon and Sun in the EME2000 frame were computed using the JPL Ephemeris DE405 and a frame-bias rotation matrix [23] that transforms the GCRF coordinates returned by the Ephemeris software into the EME2000 frame.

5.1.3. Relativistic Corrections

The curvature and dragging of space-time due to Earth's mass and rotation result in non-negligible post-Newtonian correction terms to the satellite and test mass geodesic motion. Within the context of the various forces defined earlier, these relativistic corrections are considered to be a part of the external gravitational acceleration terms. The first order relativistic acceleration correction (given below for the satellite) is given by [28]:

$$-\frac{\mu_\oplus}{\|\boldsymbol{r}_s\|_2^2}\left[\left(\frac{4\mu_\oplus}{c^2\|\boldsymbol{r}_s\|_2} - \left(\frac{\|\dot{\boldsymbol{r}}_{s_I}\|_2}{c}\right)^2\right)\hat{\boldsymbol{r}}_s + 4\left(\frac{\|\dot{\boldsymbol{r}}_{s_I}\|_2}{c}\right)^2 (\hat{\boldsymbol{r}}_s \cdot \hat{\dot{\boldsymbol{r}}}_{s_I})\hat{\dot{\boldsymbol{r}}}_{s_I}\right], \tag{9}$$

where c is the speed of light.

5.2. Environmental Disturbances

Here we consider the dominant non-conservative perturbation forces on the satellite: aerodynamic drag, radiation pressure, and magnetic torques.

5.2.1. Atmospheric Drag

Due to the highly rarefied atmosphere in LEO, the computation of aerodynamic forces differs from the standard continuum approach at aircraft flight altitudes [29]. For an altitude of 657 km, the flow regime is characterized by a freestream Kundsen number $>> 10$ placing the spacecraft within the realm of free molecular flow, specifically, sub-hyperthermal flow [29]. The discussion in [29] considers a variety of existing computational approaches to spacecraft aerodynamics, most of which employ some form of the Maxwellian gas surface interaction model. For MGRS, we implemented a simplified version of the Ray-Tracing Panel (RTP) method by decomposing the satellite surface into discrete panels and treated the incoming flow as a collimated beam of particles. That is, we do not account for multiple reflections or molecular collisions on shielded (from free-stream flow) or aft-facing surfaces. The satellite's bulk velocity with respect to the local atmosphere is approximated as:

$$\dot{\boldsymbol{r}}_{s_{I,\mathrm{rel}}} \approx \dot{\boldsymbol{r}}_{s_I} - (\boldsymbol{\omega}_{\oplus} \times \boldsymbol{r}_{s_I} + \boldsymbol{v}_w)\,,$$

where $\boldsymbol{\omega}_{\oplus}$ represents the Earth's average rotation rate and $\boldsymbol{v}_w$ is an estimate for the neutral wind velocity. Wind speeds are estimated using the Horizontal Wind Model '93[3] which is an empirical model of the horizontal neutral winds in the upper atmosphere based on data obtained from the AE-E and DE 2 satellites [30]. A set of vector spherical harmonics are used to describe the zonal and meridional wind components, including effects such as solar and geomagnetic activity. The force imparted on the i^{th} surface panel of the satellite with outward facing normal $\hat{\boldsymbol{n}}_i$ is given by:

$$\boldsymbol{F}_{\mathrm{drag}_i} = \frac{1}{2} A_i \rho \|\dot{\boldsymbol{r}}_{s_{I,rel}}\|_2^2 \Big[- C_{p_i} \hat{\boldsymbol{n}}_i + C_{\tau_i} \hat{\boldsymbol{\tau}}_i \Big], \tag{10}$$

where A_i is the (un-shielded) area of the i^{th} surface panel, ρ is the local atmospheric density, C_{p_i} and C_{τ_i} are the coefficients of pressure and shear stress respectively, and

$$\hat{\boldsymbol{\tau}}_i := \frac{(\hat{\dot{\boldsymbol{r}}}_{s_{I,\mathrm{rel}}} \times \hat{\boldsymbol{n}}_i)}{\|(\hat{\dot{\boldsymbol{r}}}_{s_{I,\mathrm{rel}}} \times \hat{\boldsymbol{n}}_i\|_2} \times \hat{\boldsymbol{n}}_i.$$

Note that the random thermal motion of the molecules is accounted for by the gas-surface interaction model and a finite molecular speed ratio (≈ 5). Based on the plots for C_p and C_τ given in [29] for a variety of molecular speed ratios, angles of incidence, and varying levels of diffuse and specular reflection using the Schaaf and Chambre gas-surface interaction model [31], (10) can be simplified to the more familiar form:

$$\boldsymbol{F}_{\mathrm{drag}_i} = -\frac{1}{2} C_d A_i \rho \|\dot{\boldsymbol{r}}_{s_{I,\mathrm{rel}}}\|_2^2 \left(\hat{\boldsymbol{n}}_i \cdot \hat{\dot{\boldsymbol{r}}}_{s_{I,\mathrm{rel}}} \right) \hat{\dot{\boldsymbol{r}}}_{s_{I,\mathrm{rel}}},$$

where $C_d \approx 3$ is the effective drag-coefficient. The aerodynamic torque due to the i^{th} surface is calculated by taking the cross-product:

$$\boldsymbol{M}_{\mathrm{drag}_i} = \boldsymbol{r}_{\mathrm{surf}_i} \times \boldsymbol{F}_{\mathrm{drag}_i},$$

where $\boldsymbol{r}_{\mathrm{surf}_i}$ is the location of the centroid of the i^{th} surface with respect to the satellite center of mass. The net force and torque were found by summing over all unshielded surfaces as determined by the RTP method. Atmospheric density was computed using the NRLMSISE 2000 atmosphere model. Efforts to

[3] Fortran code obtained from the NASA Goddard Space Flight Center online repository.

maximize accuracy for the predicted density included incorporating the effects of the solar radio flux daily ($F_{10.7}$) and 81-day average ($F_{10.7A}$) values, as well as the A_p geomagnetic index for a period up to 57 hours before the current time. For an anticipated launch date in early 2018, future solar activity predictions suggest an average 13-month smoothed $F_{10.7}$ value < 100, and an A_p geomagnetic index value ≈ 20 [32, 33]. As a conservative upper-bound, we reference the solar and geomagnetic activity recorded on April 12, 2014. This corresponds to: $F_{10.7A} = 144.4$, $F_{10.7}$(Previous daily) $= 136.9$, and A_p(daily average) $= 20$.

5.2.2. Radiation Pressure

The net radiation pressure (RP) force on the satellite can be attributed to: (a) solar radiation pressure (SRP) due to direct incidence from the Sun, and (b) Earth radiation pressure (ERP) due to reflected shortwave radiation (albedo) and re-emitted longwave infrared radiation. The resulting force from each of these sources was modeled as a sum of absorbed, specular and diffusely reflected components over all illuminated satellite surfaces. The contribution due to direct radiation from the sun on the i^{th} illuminated face is given as:

$$\boldsymbol{F}_{\mathrm{srp}_i} = -\nu \frac{P_{\mathrm{srp}} A_i \cos(\phi_{\mathrm{inc}_i})}{c} \left[2 \left(\frac{c_{rd}}{3} + c_{rs} \cos(\phi_{\mathrm{inc}_i}) \right) \hat{\boldsymbol{n}}_i + (1 - c_{rs}) \hat{\boldsymbol{s}} \right], \tag{11}$$

where P_{srp} is the incident solar irradiance measured at the satellite position (assumed constant at 1367 Wm^{-2} [34]), c is the speed of light, A_i is the illuminated area for the i^{th} satellite face (calculated using the same RTP method as for aerodynamic drag) with outward normal vector $\hat{\boldsymbol{n}}_i$, and ϕ_{inc_i} is the incidence angle between $\hat{\boldsymbol{n}}_i$ and the satellite-to-sun unit vector $\hat{\boldsymbol{s}}$. The specular (c_{rs}) and diffuse (c_{rd}) reflectivities are assumed to be equal to the GRACE solar panel coefficients (0.05 and 0.3) [35]. The parameter $\nu \in [0, 1]$ is the shadow coefficient treating Earth as the occulting body and is calculated using the algorithm in [28].

Earth radiation effects were computed using the algorithm outlined in [36] using a 5^o grid. The net shortwave (albedo) and longwave (infrared) irradiance incident at the satellite due to the j^{th} Earth element is denoted by P_{erp_j} with associated satellite-to-earth-element unit vector $\hat{\boldsymbol{s}}_j$. To avoid having to compute the radiation force due to each Earth element separately, we defined the following unit vector:

$$\hat{\boldsymbol{s}}_{\mathrm{erp}} := \frac{\sum_{j=1}^{N_{\mathrm{el}}} P_{\mathrm{erp}_j} \hat{\boldsymbol{s}}_j}{\sum_{j=1}^{N_{\mathrm{el}}} P_{\mathrm{erp}_j}},$$

where N_{el} is the total number of Earth elements in the grid. Thus, $\hat{\boldsymbol{s}}_{\mathrm{erp}}$ is a weighted (by irradiance) average of all satellite-to-Earth-element vectors incident at the satellite. The net ERP force on the i^{th} surface $\boldsymbol{F}_{\mathrm{erp}_i}$ was then calculated using (11), the net irradiance $\sum_{j=1}^{N_{\mathrm{el}}} P_{\mathrm{erp}_j}$, and the vector $\hat{\boldsymbol{s}}_{\mathrm{erp}}$. The associated torque due to the i^{th} surface is calculated as

$$\boldsymbol{M}_{\mathrm{rp}_i} = \boldsymbol{r}_{\mathrm{surf}_i} \times \left(\boldsymbol{F}_{\mathrm{srp}_i} + \boldsymbol{F}_{\mathrm{erp}_i} \right).$$

The net force and torque were found by summing over all illuminated surfaces.

5.2.3. Magnetic Torque

The magnetic field model is the World Magnetic Model 2010 (WMM 2010) which calculates the magnetic field as the gradient of a spherical harmonic representation of the magnetic potential function. The WMM 2010 model is valid until January 1, 2015 and only models the long-wavelength portion of the Earth's internal magnetic field (generated in the conducting, fluid outer core) - which represents approximately 95% of the observed magnetic field. Thus, contributions from Earth's crustal field and other disturbance effects from currents in the atmosphere are not represented. The disturbance torque on the satellite was calculated as:

$$\boldsymbol{M}_{mag} = \boldsymbol{\mu}_m \times \boldsymbol{B}, \tag{12}$$

where $\boldsymbol{\mu}_m$ is the residual magnetic moment vector, and $\boldsymbol{B}$ is the local Earth magnetic field vector. For simulating worst case conditions, we assumed a residual magnetic moment magnitude of 0.1 Am^2.

5.3. Stiffness Disturbance

In this section we detail the coupled disturbance forces between the satellite and test mass. The two primary contributions to this disturbance stem from electromagnetic stiffness and mass attraction. The electromagnetic stiffness acceleration $\boldsymbol{f}_{sp_{em}}$, is modeled as an unstable linear spring:

$$\boldsymbol{f}_{sp_{em}} = K_{em}\left(\boldsymbol{r}_{sp} - \boldsymbol{r}_{eq_e}\right), \tag{13}$$

where $\boldsymbol{r}_{eq_e}$ defines an equilibrium point with respect to the satellite center of mass, and K_{em} is the electromagnetic gradient. As in [24], we assume that the equilibrium point for the model given in (13) is the center of the DOSS cavity (this is a reasonable assumption for a spherical test mass contained within a symmetric housing). That is, $\boldsymbol{r}_{eq_e}$ is the vector from the center of mass of the satellite to the center of the DOSS cavity. Additionally, since the test mass has a diameter of 2.5 cm and the internal dimensions of the DOSS cavity correspond to a 5 cm cube, we have a housing gap on the order of 12.5 mm. A reasonable estimate for K_{em} based on the calculations in [24] for this housing gap is given by $3 \cdot 10^{-7} I_3$ s^{-2}. The off-diagonal elements for K_{em} are expected to be negligible due to inherent symmetry of the spherical test mass and caging environment.

The mass attraction disturbance is modeled more precisely by decomposing the satellite into a cuboid mesh. The mesh is more coarse (order of 20 cm cubes) further away from the DOSS cavity and reduces down to 5 cm cubes near the cavity. The solar panels are treated as thin plates. The i^{th} cuboid is assumed to be a block with uniform density with mass m_i and inertia matrix J_i (expressed in the satellite body frame), located at a point $\boldsymbol{r}_{b_i}$ with respect to the satellite center of mass; for simplicity a symmetrical mass distribution is assumed about the body $x-$axis. Given the position of the test mass with respect to the satellite center of mass ($\boldsymbol{r}_{sp}$), the net gravitational potential at that location due to the satellite is given by the sum of the gravitational potential due to each cuboid, computed using the generalization of MacCullagh's 2^{nd} order formula [37, 38]:

$$U = \sum_{i=1}^{N_b} \frac{G m_i}{\|\boldsymbol{r}_{bp_i}\|_2} + \frac{G}{2\|\boldsymbol{r}_{bp_i}\|_2^3}\left(\text{Trace}(J_i) - 3\hat{\boldsymbol{r}}_{bp_i} \cdot J_i \hat{\boldsymbol{r}}_{bp_i}\right), \tag{14}$$

where N_b is the total number of cuboids in the mesh, and $\boldsymbol{r}_{bp_i} = \boldsymbol{r}_{sp} - \boldsymbol{r}_{b_i}$ is the location of the test mass with respect to the i^{th} cuboid. The force is then given as the negative gradient of the above expression. The contributions to the test mass and satellite accelerations were computed using an extension of the 3^{rd} body formula given in (8).

5.4. Simulation Results

We are now ready to compute the expected disturbance profile for the MGRS satellite aligned with the LORF corresponding to a mean 657 km Sun-synchronous $0600:1800$ dawn/dusk orbit.

The results of the disturbance simulations are presented in Figure 3.

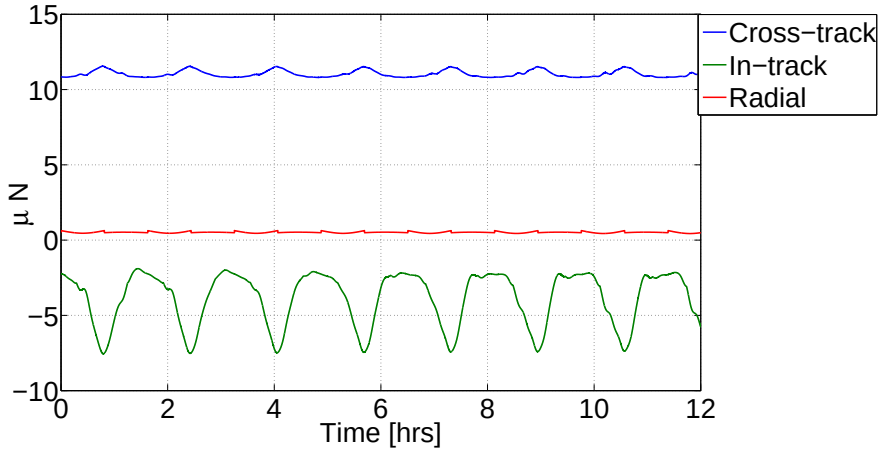

(a) Sum of aerodynamic drag and RP forces; direct SRP forces dominate the cross-track axis while aerodynamic drag and ERP constitute the primary disturbances in the in-track and radial directions respectively.

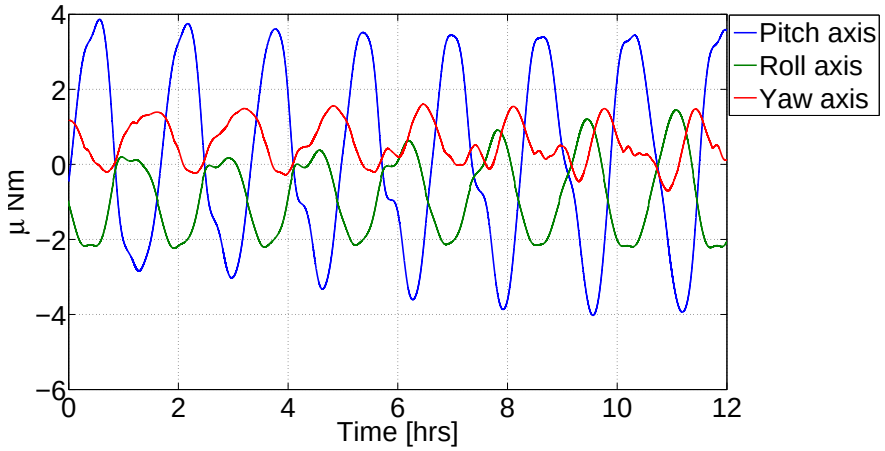

(b) Sum of all environmental disturbance torques; the primary disturbance is due to the residual magnetic moment.

Figure 3: Environmental disturbances.

In Figure 3a, notice that the dominant disturbance is in the cross-track direction and is due to the direct SRP force. This is expected since the Sun lies roughly normal to the plane of a dawn/dusk Sun-synchronous orbit (particularly during periods where the Earth is crossing the Vernal Equinox axis as is the case near April). The fluctuations in this force are due to cross-track aerodynamic drag as a result of a co-rotating atmosphere and zonal atmospheric winds. The dominant disturbance in the in-track axis is atmospheric drag and varies roughly between $2 - 8$ μN. The radial axis experiences very little disturbance (< 1 μN) and primarily consists of ERP forces.

Figure 3b shows the net disturbance torques due to all environmental sources. The dominant effect is the magnetic disturbance torque; aerodynamic torques were less than 0.5 μNm about the yaw axis, and RP torques were less than 0.5 μNm in roll and between ± 0.04 μNm in the yaw axis. The gravity gradient torque was essentially negligible (under the assumption of small roll and pitch angles). The magnetic disturbance torque was calculated based on a randomly generated direction for the magnetic dipole. A conservative upper bound for this disturbance is given by the product of the dipole strength (< 0.1 Am^2) with the worst case magnetic intensity at this altitude (< 49 μT). This yields a worst case magnetic disturbance torque on

the order of 4.9 μNm.

Using the environmental disturbance estimates, we can derive a control force and torque envelope required for adequate drag-free and attitude control. In particular, the propulsion assembly should be able to generate torques up to ± 10 μNm (based on a factor of safety of two with respect to the magnetic torques). For forces, we require controllability in the ranges

- $[-30, 10]$ μN for cross-track,
- $[-20, 20]$ μN for in-track, and
- $[-10, 10]$ μN for the radial axis.

For a stabilized (with respect to LORF) attitude, the force controllability ranges above coincide with the x, y and z axes of the satellite. This force and torque envelope is used to generate a feasible configuration for the propulsion assembly as discussed in Section 6.1. and Appendix 11.2.

Having obtained a comprehensive characterization of the expected force and torque disturbances for MGRS, we are now ready to formalize the drag-free and attitude control problems.

6. Control Design

The drag-free and and attitude control design for MGRS must accomplish the following goals within the science frequency band $\mathcal{B}$:

- restrict the non-gravitational acceleration ASD on the proof-mass to be below 10^{-12} ms$^{-2}/\sqrt{\text{Hz}}$,
- restrict the ASD for the Euler angles to be below 0.1 rad$/\sqrt{\text{Hz}}$,
- restrict the ASD for the Euler angular rates to be below 100 μrad s$^{-1}/\sqrt{\text{Hz}}$, and
- restrict the ASD for the Euler angular accelerations to be below 0.4 μrad s$^{-2}/\sqrt{\text{Hz}}$.

The derivation of the last three requirements above are detailed in the attitude control subsection. As the spacecraft possesses a nominal spin (due to the LORF orientation), the drag-free and attitude control objectives become coupled. We present a *decoupled* control approach where the drag-free controller is designed first by assuming a stabilized three-axis attitude. The assumptions required to formulate this controller then lead to performance bounds on the attitude control subsystem. The primary sensors for the control systems are the DOSS, star-trackers, and a GNSS receiver (used to estimate the LORF). The actuator is a FEEP micropropulsion system that provides full three-axis force and torque compensation. We do not use any momentum or magnetic based attitude control during the drag-free operational mode to avoid introducing additional disturbances on the test mass. The selection of this propulsion system is guided by the disturbance envelope calculations and is detailed first.

6.1. Thruster Selection and Configuration

As mentioned earlier, the ability to generate a high precision drag-free environment for the test mass is dependant on the quality of the micropropulsion system. For MGRS, a variety of propulsion options were considered:

- Cold-gas: Both GPB and GAIA successfuly used proportional cold-gas thrusters. The GAIA micropropulsion subsystem consists of 12 micro-thrusters each with closed-loop thrust control at 40 Hz, thrust controllability between 1-1000 μN, thrust resolution of 0.1 μN, and thrust noise < 0.1 μN$/\sqrt{\text{Hz}}$ [22, 39]. These thrusters will also be flown on the upcoming LPF and CNES Microscope [12] missions. While these thrusters would be ideal for drag-free control, the low specific impulse (I_{sp}) of cold gas (< 65 s reported by GAIA) and gas leakage would severely limit mission lifetime. As MGRS is a small microsatellite, it is unable to accomodate large propellant tanks. The use of on/off cold gas thrusters within a bang-bang and bang-off-bang control scheme was also considered. This method

was eventually abandoned due to: (a) excessive actuation for small deadbands, and (b) unacceptable drag-free performance when using a larger deadband (due to the stiffness coupling).

- Electric Propulsion: Low-thrust electric propulsion is characterized by average $I_{sp} > 2500$ s, and low mass and volume requirements. Several options were considered including the Giessen μN RIT ion thrusters [40], Busek Electrospray thrusters [41], and ALTA FT-150 FEEP thrusters [42, 43]. Several other new electric propulsion technologies are reported in [44], however most are still in early development phase. While electric propulsion certainly meets the propellant consumption and volume restrictions, most current technologies require too much power. For instance, two Giessen μN ion engines operating at 300 μN each would consume $\approx$ 100 W (including losses) [45]. This is the primary reason a low altitude mission was declared infeasible for MGRS.

Recent communication with ALTA SpA on their FT-150 FEEP thrusters yielded the data given in Table 2.

Characteristic	Comments	Value
Power	4 thruster cluster at 100 μN/thruster	< 40 W
	Power Control Unit (PCU)	< 10 W
	Neutralizer	< 4.5 W
Thrust range		$0.1 - 150$ μN
Thrust resolution		0.1 μN
I_{sp}		$3000 - 4500$ s
Thrust noise	0.01-1 Hz	< 0.1 μN/$\sqrt{\text{Hz}}$
Time response	Rise time ($31 - 60$ μN)	< 80 ms
TRL		7

Table 2: ALTA FT-150 FEEP Characteristics

Additionally, the noise profile for each individual thruster is given in the following plot [46].

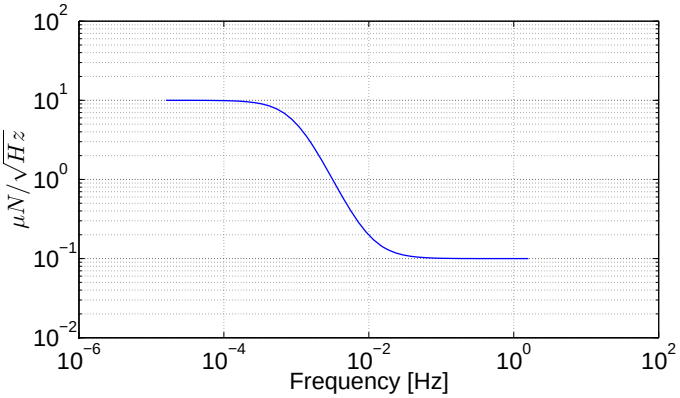

Figure 4: Individual thrust noise unilateral ASD (including quantization error noise due to 0.1μN at 10 Hz).

The disturbance envelope calculated in Section 5.4. was used within a convex optimization algorithm to obtain a *feasible* thruster configuration that guarantees the ability to counteract all expected disturbance forces and torques. This procedure yielded a thruster configuration that utilizes 3 clusters with 3 thrusters per cluster, operating at < 55 μN per thruster (see Appendix 11.2.). With a reduced number of thrusters per cluster and smaller thrust load, the FT-150 FEEP thrusters are a promising choice for this mission. The rise time reported in Table 2 corresponds to a fairly large step of 30 μN whereas smooth operation is anticipated. Accordingly, the thrusters are modeled with first order dynamics having a rise time of 50 ms (time constant

$\tau_t = 26$ ms) with a steady state gain of unity:

$$f_t(s) = \frac{1}{\tau_t s + 1}. \tag{15}$$

In future work, we will expand upon this model to include uncertainties in the steady-state error. To generalize the individual thruster noise in terms of the net force and torque noise for each axis (thereby implicitly accounting for cross effects), the noise curve in Figure 4 is scaled by the l^1 norm of the corresponding row in the configuration matrix (see Appendix 11.2.).

6.2. Drag-Free Control

The drag-free performance objective for MGRS is to achieve a residual acceleration noise floor for the test mass less than 10^{-12} ms$^{-2}/\sqrt{\text{Hz}}$ within the science frequency band $\mathcal{B}$. To help formalize this objective within a control framework, consider the normalized version of (2a). The net non-gravitational normalized force $\boldsymbol{f}_{ng}$ on the test mass can be written as

$$\boldsymbol{f}_{ng} = \boldsymbol{f}_{dp} + \boldsymbol{f}_{sp}. \tag{16}$$

As mentioned earlier, control feedback cannot mitigate the effect of the direct perturbations on the test mass $\boldsymbol{f}_{dp}$. The dominant contributions to the stiffness disturbance $\boldsymbol{f}_{sp}$ are electromagnetic and mass attraction effects. While the non-linear summation in (14) is a reasonable approximation for simulating the mass attraction disturbance, it is not in a convenient form for drag-free control design. Accordingly, we first generalize the electromagnetic and mass attraction disturbances by defining a point $\boldsymbol{r}_{eq}$ with respect to the satellite center of mass, hereby referred to as the "control center," and *approximate* $\boldsymbol{f}_{sp}$ about this point as follows:

$$\boldsymbol{f}_{sp} \approx \underbrace{\left(K_{em} + K_{gg_{|eq}}\right)}_{:=K} (\boldsymbol{r}_{sp} - \boldsymbol{r}_{eq}) + \bar{\boldsymbol{f}}_{sp}, \tag{17}$$

where $\bar{\boldsymbol{f}}_{sp}$ is the residual bias due to the electromagnetic[4] and self-gravitational forces at $\boldsymbol{r}_{eq}$, $K_{gg_{|eq}}$ is the self-gravity gradient at $\boldsymbol{r}_{eq}$, and K is the net coupled force gradient. Note that $\boldsymbol{r}_{eq}$ represents a design choice whose selection is motivated by minimizing both the bias and the net gradient at this point. A similar design philosophy is portrayed in [47] where the authors modify the satellite's inertial properties to minimize the self-gravity gradient at a given point. Guided by the same design objective as in [47], by testing a few different points within the DOSS cavity, we selected the control center to be located 1.74 mm along the negative $x-$axis with respect to the center of the DOSS cavity. Using the cuboid mesh described in Section 5.3., we deduce that $\boldsymbol{r}_{eq} = [1.5, 0, 0]^T$ cm, the net bias force $\bar{\boldsymbol{f}}_{sp}$ is $[4.722 \cdot 10^{-10}; 0; 0]$ ms^{-2}, and the self-gravity gradient $K_{gg_{|eq}}$ was computed to be:

$$K_{gg_{|eq}} \approx \begin{bmatrix} 3.987178 & 0 & 0 \\ 0 & 3.29246 & 0 \\ 0 & 0 & 3.35296 \end{bmatrix} \cdot 10^{-7}\text{s}^{-2},$$

where the off-diagonal terms are negligible (order 10^{-18}). For control design, we used a more conservative upper bound $K = 10^{-6} I_3$ s^{-2}.

Note that the stiffness interactions between the satellite and test mass are in general quite difficult to predict on ground and the design model described in (17) is an approximation only. The final bias and stiffness gradients must be estimated online during on-orbit calibration [48].

[4]The residual electromagnetic bias force at $\boldsymbol{r}_{eq}$ is equal to $K_{em}\left(\boldsymbol{r}_{eq} - \boldsymbol{r}_{eq_e}\right)$.

Let $\boldsymbol{r}_c := \boldsymbol{r}_{sp} - \boldsymbol{r}_{eq}$ denote the position of the test mass with respect to the control center $\boldsymbol{r}_{eq}$, hereby referred to as the "drag-free control error". Using (17), the expression for the non-gravitational accelerations $\boldsymbol{f}_{ng}$ becomes:

$$\boldsymbol{f}_{ng} = \boldsymbol{f}_{dp} + K\boldsymbol{r}_c + \bar{\boldsymbol{f}}_{sp}.$$

Given our upper bound for $\boldsymbol{f}_{dp}$ ($< 4{\cdot}10^{-13}$ ms$^{-2}/\sqrt{\text{Hz}}$ in all axes), and K ($< 10^{-6}$ s^{-2} along the diagonal), the drag-free performance requirement can be *equivalently* re-stated as the following *translational* control objective:

$$\widetilde{\boldsymbol{r}}_c(f) < 10^{-7}\ \text{m}/\sqrt{\text{Hz}},\ f \in \mathcal{B}. \tag{18}$$

Note that the above specification applies to all three directions. Using the definition of the control error, (4) may be re-written as follows:

$$\ddot{\boldsymbol{r}}_{c_B} = \delta\boldsymbol{f}_{eq} + \delta\boldsymbol{f}_c + \delta\boldsymbol{f}_g + \delta\boldsymbol{f}_{sp} + \delta\boldsymbol{f}_p + \boldsymbol{u}_T \tag{19}$$

where,

$$\delta\boldsymbol{f}_{eq} := -\left[\dot{\boldsymbol{\omega}} \times \boldsymbol{r}_{eq} + \boldsymbol{\omega} \times (\boldsymbol{\omega} \times \boldsymbol{r}_{eq})\right] \tag{20a}$$

$$\delta\boldsymbol{f}_c := -\left[\dot{\boldsymbol{\omega}} \times \boldsymbol{r}_c + 2\boldsymbol{\omega} \times \dot{\boldsymbol{r}}_{c_B} + \boldsymbol{\omega} \times (\boldsymbol{\omega} \times \boldsymbol{r}_c)\right] \tag{20b}$$

$$\delta\boldsymbol{f}_g := \boldsymbol{f}_{gp} - \boldsymbol{f}_{gs} \tag{20c}$$

$$\delta\boldsymbol{f}_{sp} := \underbrace{\left(1 + \frac{m_b}{m_s}\right)}_{:=m^{-1}} \boldsymbol{f}_{sp} = m^{-1}\left(K\boldsymbol{r}_c + \bar{\boldsymbol{f}}_{sp}\right) \tag{20d}$$

$$\delta\boldsymbol{f}_d := \boldsymbol{f}_{dp} - \boldsymbol{f}_{ds} \tag{20e}$$

$$\boldsymbol{u}_T := -\boldsymbol{f}_{cs} \tag{20f}$$

Thus, $\delta\boldsymbol{f}_{eq}$ and $\delta\boldsymbol{f}_c$ act as "fictitious" disturbances due to the Coriolis and centrifugal accelerations from $\boldsymbol{r}_{eq}$ and $\boldsymbol{r}_c$, $\delta\boldsymbol{f}_g$ and $\delta\boldsymbol{f}_d$ are the differential gravity and direct perturbation disturbances respectively, and $\boldsymbol{u}_T$ is the normalized control thrust. It is important to note that the bias disturbance $m^{-1}\bar{\boldsymbol{f}}_{sp}$ is unavoidable in pure drag-free mode (as opposed to accelerometer drag-free mode [24]) and will lead to a steady state perturbation of the overall satellite/test mass assembly. In order to use linear control design techniques and decouple the attitude and translational control problems, the following simplifications are employed:

- Stabilized attitude: $\dot{\boldsymbol{\omega}} \approx \boldsymbol{0}$, $\boldsymbol{\omega} \approx \bar{\boldsymbol{\omega}}$, where $\bar{\boldsymbol{\omega}}$ is a constant assumed spin rate. For MGRS, this corresponds to the satellite's mean motion, i.e. $\bar{\boldsymbol{\omega}} := [\bar{n}, 0, 0]^T$, where $\bar{n}$ is the mean motion of the satellite.
- Neglect the term $\delta\boldsymbol{f}_g$: The differential gravitational acceleration due to a spherical Earth between two points < 0.1 μm apart at an altitude of 657 km is in the order of 10^{-13} ms^{-2}, and can be safely neglected.

Leveraging the above simplifications, (19) can be re-written as a linear time invariant MIMO plant. Let $\bar{\Omega}$ be the skew-symmetric form for $\bar{\boldsymbol{\omega}}$. Then, define the following state vector:

$$\boldsymbol{X} := \begin{bmatrix} \boldsymbol{r}_c \\ \dot{\boldsymbol{r}}_{c_B} \end{bmatrix}.$$

Equation (19) can now be re-written as the following MIMO system:

$$\begin{aligned} \dot{\boldsymbol{X}} = \begin{bmatrix} \dot{\boldsymbol{r}}_{c_B} \\ \ddot{\boldsymbol{r}}_{c_B} \end{bmatrix} &\approx \underbrace{\begin{bmatrix} O_3 & I_3 \\ m^{-1}K - \bar{\Omega}^2 & -2\bar{\Omega} \end{bmatrix}}_{A} \boldsymbol{X} + \underbrace{\begin{bmatrix} O_3 \\ I_3 \end{bmatrix}}_{B} \left(\boldsymbol{u}_T + m^{-1}\bar{\boldsymbol{f}}_{sp} + \delta\boldsymbol{f}_d + \delta\boldsymbol{f}_{eq}\right), \\ \boldsymbol{r}_{c_B} &= \underbrace{\begin{bmatrix} I_3 & O_3 \end{bmatrix}}_{C} \boldsymbol{X} + \boldsymbol{\eta}, \end{aligned} \tag{21}$$

where O_3 is a 3×3 matrix of zeros, and $\boldsymbol{\eta}$ represents the measurement noise from the DOSS. From laboratory experiments, the DOSS noise may be characterized by the ASD shown in Figure 5 [49].

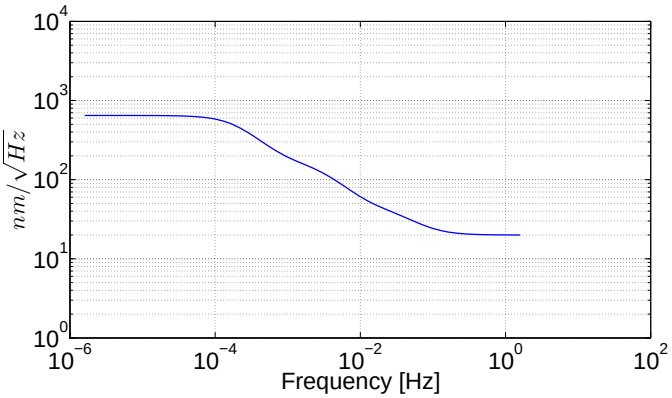

Figure 5: Single axis upper bound for the DOSS unilateral noise ASD; the other two axes are anticipated to have the same upper bound.

In order to meet the objective given in (18) a variety of control methodologies were considered. For instance, [1] discusses an on/off based limit cycle controller. The GOCE drag-free control design employs discrete control techniques including an online disturbance estimator [21] . In [50, 51, 52], the authors upper bound the disturbance ASDs and employ $H_\infty-$ control techniques, and [53] presents a mixed $\mu-$synthesis (see [54]) approach by maximizing the performance weights subject to the structured singular value constraints for robust stability and performance, thereby dispelling the need to fashion performance weights manually. For obtaining a preliminary controller here using the disturbance, noise, and performance ASDs, we employ the $H_\infty-$ control design methodology [55].

To begin, note that the primary input disturbances in (21) stem from the direct disturbance forces on the satellite, i.e. the component $\boldsymbol{f}_{ds}$ in $\delta\boldsymbol{f}_d$. This primarily consists of: thruster noise, aerodynamic drag, and RP. Inspite of the clear periodic nature of the disturbances as seen in Figure 3a, in order to derive a controller within a unified spectral density framework, we must model the disturbance as having a high noise amplitude at low frequency as shown in Figure 6.

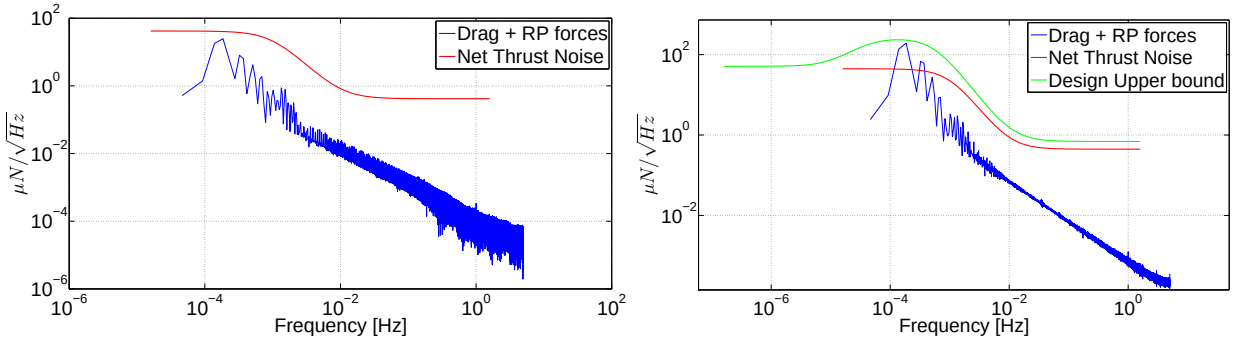

(a) $x-$ axis. (b) $y-$ axis.

Figure 6: Unilateral ASDs for input disturbances; DC trend removed for Drag + RP curves and design weight for $y-$ axis shaped to capture resonance near orbital frequency.

Figure 6 shows that the thrust noise ASD dominates the environmental disturbance ASD for the $x-$axis (the $z-$axis is very similar). This is expected since the disturbances in the x and z axes (primarily SRP and ERP) do not show much variation over an orbit, and can be easily bounded by the low frequency asymptote of the thrust noise ASD. For the $y-$axis however, we used the upper bound given by the green

curve which also captures the resonance effects near the orbital frequency. Finally, we scaled the normalized (by satellite mass) thrust noise curves in Figure 6 by an additional factor of two to also account for the perturbation due to $\delta \boldsymbol{f}_{eq}$. This places an implicit bound on the rotational dynamics embedded within the translational equations of motion and will be used to derive performance bounds for the attitude controller. The generalized plant/drag-free controller feedback system is shown in Figure 7.

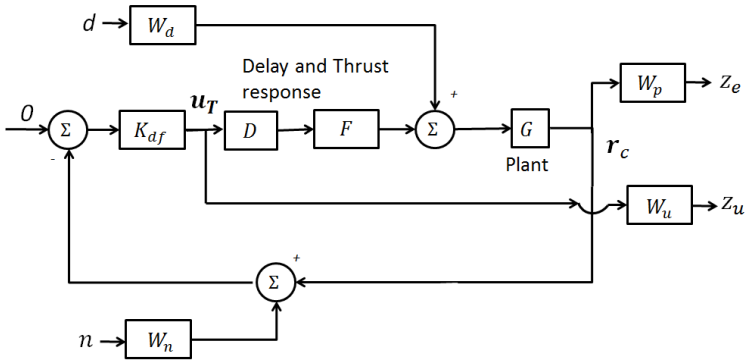

Figure 7: Drag-free control loop with normalized exogenous inputs d and n and performance variables z_e and z_u.

In the figure above, $W_d = \text{diag}(2w_{d_x}, 2w_{d_y}, 2w_{d_z})$ where w_{d_i} is the normalized input disturbance weight for the i^{th} axis (Figure 6), $W_n = \text{diag}(w_n, w_n, w_n)$ where w_n is the DOSS noise ASD (Figure 5), K_{df} is the drag-free controller, $D = \text{diag}(d_t, d_t, d_t)$ where d_t is a first order Padé approximation of a 150 ms delay (50 ms effective sampling delay and 100 ms for one sample period hold for data processing, thrust allocation, etc.), $F = \text{diag}(f_t, f_t, f_t)$ where f_t is the first order model for the FEEP thrusters[5], and $W_p = \text{diag}(w_p, w_p, w_p)$ and $W_u = \text{diag}(w_u, w_u, w_u)$ model the inverse of the allowed spectral densities for the drag-free error and control signals respectively. The exogenous inputs d and n represent the normalized input disturbances and noise (i.e. white noise with a spectral density upper bounded by one), and the outputs z_e and z_u represent the normalized ASDs for the drag-free error and control signals. Both w_p and w_u are plotted in Figure 8.

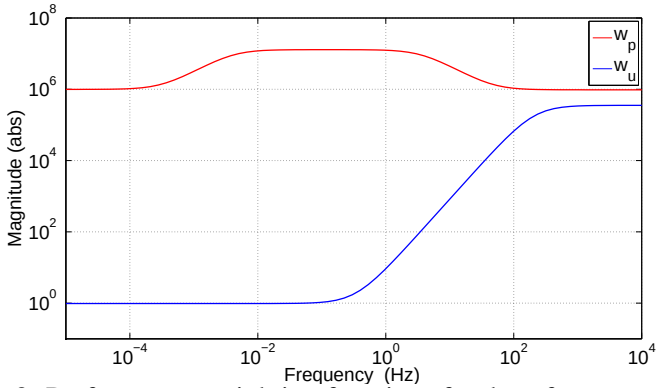

Figure 8: Performance weighting functions for drag-free control loop.

The closed-loop transfer functions from the normalized input disturbance and noise to the performance

[5]Note that we neglect differences between *individual* thruster time reponses and model the net force in each axis to have the same first order response.

outputs z_e and z_u are given by:

$$\begin{bmatrix} z_e \\ z_u \end{bmatrix} = \underbrace{\begin{bmatrix} W_p \underbrace{(I + GFDK_{df})^{-1}}_{S_o} GW_d & -W_p \underbrace{S_o GFDK_{df}}_{T_o} W_n \\ -W_u \underbrace{(I + K_{df}GFD)^{-1}}_{S_I} K_{df}GW_d & W_u S_I K_{df} W_n \end{bmatrix}}_{:=N} \begin{bmatrix} d \\ n \end{bmatrix}, \tag{22}$$

where S_o and T_o are the output sensitivity and complementary sensitivity functions respectively, and S_I is the input sensitivity. Note that the above definitions highlight the fact that the effective plant transfer function is given by GFD. The stacked H_∞ objective is now formalized as:

$$\|N\|_\infty < 1, \tag{23}$$

where $\|N\|_\infty$ is defined as the maximum singular value of N over all frequencies. The use of the $H_\infty-$norm is justified in the sense that it ensures that the ASDs for the drag-free control error and control signal are below the desired bounds (given by $1/w_p$ and $1/w_u$) at all frequencies. The design of the performance weighting functions was guided by some fundamental limitations in the generalized plant/controller structure shown in Figure 7.

At low frequencies where $\sigma(S_o) << 1$ and $\sigma(T_o) \approx 1$, the control error performance is limited by the DOSS noise which is why the performance weight w_p is relaxed for frequencies below $\mathcal{B}$. Within $\mathcal{B}$ itself, the jitter from DOSS noise is negligible (on the order of 20 nm/$\sqrt{\text{Hz}}$). Here, the primary constraint stems from the rejection of input disturbances, and w_p within the science band is adjusted accordingly to reflect the control objective given in (18). From Figure 7 we note that the open loop transfer function from the normalized disturbance to the performance output z_e is given by $W_p G W_d$. The frequency at which $\bar{\sigma}(W_p G W_d)$ crosses one from above defines a lower bound on the closed-loop bandwidth for S_o (defined as the frequency at which $\bar{\sigma}(S_o) = 1$ from below), and is equal to 0.0571 Hz. Additionally, as the drag-free loop runs at 10 Hz (limited by thruster command rate) and accounting for an additional delay margin of 100 ms, we also desire an upper bound (at most 1 Hz) on the control bandwidth. This is the purpose of the performance weighting function W_u which aggressively penalizes control past 0.1 Hz. Fine tuning of the performance weighting functions was accomplished by considering fundamental limitations on the weighted sensitivity and complementary sensitivity peaks as given in [55]. The results of the $H_\infty-$optimization are summarized in Figure 9 and the text thereafter.

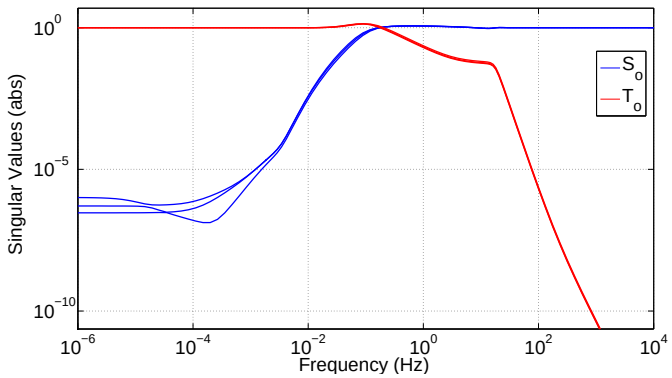

Figure 9: Closed-loop output sensitivity and complementary sensitivity singular values; closed-loop bandwidth: 0.154 Hz.

Figure 9 shows the singular values of the closed-loop output sensitivity S_o and complementary sensitivity T_o for the complete MIMO system; the closed-loop sensitivity bandwidth is 0.154 Hz. The optimization

yielded the value $\|N\|_\infty = 0.8919 < 1$ which confirms that the controller meets the performance specifications dictated by the optimization objective in (23). This peak is located at 0.004 Hz which is below the science band $\mathcal{B}$; the small margin here can be attributed to the $1/f$ pink noise characteristic of the DOSS measurements.

It is now instructive to consider some of the implications of the simplifications made in order to obtain (21). In particular, we assumed a nominal spin (about the $x-$axis), negligible angular acceleration, and a nominal value for the stiffness gradient K. In its full generality, the state matrix A in (21) should be

$$\begin{bmatrix} O_3 & I_3 \\ m^{-1}K - \Omega^2 - \dot{\Omega} & -2\Omega \end{bmatrix},$$

where Ω and $\dot{\Omega}$ are the skew-symmetric forms for $\boldsymbol{\omega}$ and $\dot{\boldsymbol{\omega}}$ respectively. By setting bounds on $\|\boldsymbol{\omega} - \bar{\boldsymbol{\omega}}\|_\infty$, $\|\dot{\boldsymbol{\omega}}\|_\infty$, and the diagonal entries of K, an uncertainty set for the nominal plant dynamics may be derived using the techniques described in [56]. This decomposition allows the use of control synthesis techniques such as $\mu-$synthesis to yield a *robust* controller. However, it should be noted that the angular rate and acceleration terms in the state matrix are time-varying. Thus, a rigorous stability and performance analysis must leverage tools from Lyapunov stability theory for uncertain systems [57], and time-varying structural perturbation techniques presented in [58]. For this preliminary H_∞ controller, we neglected the time-varying characteristic and instead, ran a Monte Carlo simulation by sampling $\boldsymbol{\omega}$ ($\|\boldsymbol{\omega} - \bar{\boldsymbol{\omega}}\|_\infty < 4 \cdot 10^{-3}$ rad/s), $\dot{\boldsymbol{\omega}}$ ($\|\dot{\boldsymbol{\omega}}\|_\infty < 4 \cdot 10^{-3}$ rad/s^2), and K (diagonal entries between $[0.5, 1.5] \cdot 10^{-6}$ s^{-2}) and evaluated the closed-loop stability properties and the performance measure $\|N\|_\infty$. The closed-loop system was found to be stable in all cases and satisfied the performance bound in (23). In future work, we will address the robust stability and performance characteristics in more detail.

6.3. Attitude Control

Given the parameterization of the attitude with respect to the LORF in terms of the Euler angles (ψ, θ, ϕ), a first order approximation for the angular velocity $\boldsymbol{\omega}$ is given by:

$$\boldsymbol{\omega} \approx \begin{bmatrix} \dot{\theta} + \bar{n} \\ \dot{\phi} - \bar{n}\psi \\ \dot{\psi} + \bar{n}\phi \end{bmatrix}, \tag{24}$$

where $\bar{n}$ is the mean motion, and second order terms in the Euler angles and their rates are neglected. Applying a first order approximation to the gravity gradient disturbance torque in (7), the Euler equations in (5a) are rewritten as follows:

$$\ddot{\theta} + 3\bar{n}^2 c\theta = \frac{1}{J_x}\left(M_{c_x} + M_{d_x}\right) \tag{25a}$$

$$\ddot{\phi} + 4a\bar{n}^2\phi + \bar{n}\dot{\psi}(a-1) = \frac{1}{J_y}\left(M_{c_y} + M_{d_y}\right) \tag{25b}$$

$$\ddot{\psi} + b\bar{n}^2\psi + \bar{n}\dot{\phi}(1-b) = \frac{1}{J_z}\left(M_{c_z} + M_{d_z}\right), \tag{25c}$$

where J_x, J_y and J_z are the principal moments of inertia (which coincide with the satellite body frame due to symmetry in the mass distribution), and

$$c := \frac{J_y - J_z}{J_x} = 0.02477$$

$$a := \frac{J_x - J_z}{J_y} = -0.023925$$

$$b := \frac{J_x - J_y}{J_z} = -0.04867.$$

Prior to discussing the control objectives, notice the following observations:

- The pitch equation decouples from the other two axes and has pure oscillatory poles at a frequency of $0.23 \cdot 10^{-3}$ rad/s which is quite close to the orbital frequency ($1.073 \cdot 10^{-3}$ rad/s).
- The roll and yaw coupled equations possess two sets of pure oscillatory poles at frequencies of $\{1.032, 0.0762\} \cdot 10^{-3}$ rad/s, the first being quite close to the orbital frequency.

Both points above highlight the need for sufficient control authority near the orbital frequency, and thereby motivate the design of the input disturbance weighting functions for H_∞ control synthesis. The design of the attitude controller was motivated by the following points:

Disturbances: Similar to the analysis for the drag-free controller, the ASDs due to environmental torques are computed and compared with the net torque disturbance due to thruster noise. These results are shown in Figure 10. The input weight used for design (shown in green) captures resonances near the orbital frequency due to environmental effects and thruster noise at higher frequencies.

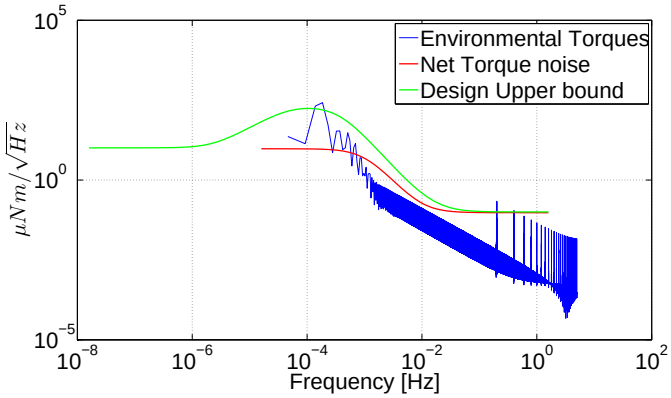

Figure 10: Unilateral ASDs for input disturbances torques along Pitch axis (other axes are similar); DC trend removed for environmental disturbance torques.

Noise: The Euler angles are estimated by differencing the inertial attitude given by the star-trackers and the estimate of the LORF derived from GNSS navigation solutions. We assume that the GNSS solutions are sampled at 1 Hz, and corrupted with Gaussian noise with standard deviation in position ν_r of 10 m, and in velocity ν_v of 5 cm/s. The transformation matrix R_o from the ECI to LORF frame is defined as:

$$R_o = \begin{bmatrix} \hat{\boldsymbol{i}}_o & \hat{\boldsymbol{j}}_o & \hat{\boldsymbol{k}}_o \end{bmatrix}^T = \left[\frac{\boldsymbol{r}_s \times \dot{\boldsymbol{r}}_{s_I}}{\|\boldsymbol{r}_s \times \dot{\boldsymbol{r}}_{s_I}\|_2}, \quad \hat{\boldsymbol{k}}_o \times \hat{\boldsymbol{i}}_o, \quad \frac{-\boldsymbol{r}_s}{\|\boldsymbol{r}_s\|_2} \right]^T.$$

Using the noise corrupted measurements, the estimate $\hat{R}_o$ may be written as:

$$\hat{R}_o \approx (I_{3\times 3} + \Delta\varepsilon)\, R_o,$$

where $\Delta\varepsilon$ is the skew-symmetric form of the vector $\boldsymbol{\varepsilon} := [\varepsilon_x, \varepsilon_y, \varepsilon_z]^T$, which represents infinitesimal rotational errors about the nominal orbital frame axes. For a near-circular orbit, this vector may be approximated as:

$$\begin{bmatrix} \varepsilon_x \\ \varepsilon_y \\ \varepsilon_z \end{bmatrix} \approx \begin{bmatrix} \dfrac{\delta\dot{\boldsymbol{r}}_{s_I} \cdot \hat{\boldsymbol{k}}_o}{\|\dot{\boldsymbol{r}}_{s_I}\|_2} + \dfrac{\delta\boldsymbol{r}_s \cdot \hat{\boldsymbol{j}}_o}{\|\boldsymbol{r}_s\|_2} \\ -\dfrac{\delta\boldsymbol{r}_s \cdot \hat{\boldsymbol{i}}_o}{\|\boldsymbol{r}_s\|_2} \\ -\dfrac{\delta\dot{\boldsymbol{r}}_{s_I} \cdot \hat{\boldsymbol{i}}_o}{\|\dot{\boldsymbol{r}}_{s_I}\|_2} \end{bmatrix},$$

where $\delta \boldsymbol{r}_s$ and $\delta \dot{\boldsymbol{r}}_{s_I}$ are the errors in absolute position and velocity. The star-tracker measurements are sampled at 2 Hz and corrupted with Gaussian noise with standard deviation ν_s of 20" (0.00556^o). Assuming an on-board Extended Kalman Filter (EKF) running at 5 Hz, the net unilateral noise ASDs for the post-EKF Euler angles estimates may be approximated as:

$$\begin{aligned}\begin{bmatrix}\widetilde{\theta}(f)\\ \widetilde{\phi}(f)\\ \widetilde{\psi}(f)\end{bmatrix} &\approx \sqrt{2T_{ekf}}\begin{bmatrix}\sqrt{\left(\frac{\nu_v}{\|\dot{\boldsymbol{r}}_{s_I}\|_2}\right)^2+\left(\frac{\nu_r}{\|\boldsymbol{r}_{s_I}\|_2}\right)^2+\nu_s^2}\\ \sqrt{\left(\frac{\nu_r}{\|\boldsymbol{r}_{s_I}\|_2}\right)^2+\nu_s^2}\\ \sqrt{\left(\frac{\nu_v}{\|\dot{\boldsymbol{r}}_{s_I}\|_2}\right)^2+\nu_s^2}\end{bmatrix}\\ &\approx \begin{bmatrix}61.475\\ 61.475\\ 61.475\end{bmatrix}\ \mu\text{rad}/\sqrt{\text{Hz}},\ f\leq 2.5\text{Hz},\end{aligned} \tag{26}$$

where $T_{ekf} = 0.2$ s is the sample time of the EKF. That is, we have assumed that the EKF yields a noise level that is lower than the sum of the expected noise floors due to each individual source ($< 9.6\ \mu\text{rad}/\sqrt{\text{Hz}}$ up to 0.5 Hz due to GNSS, and $< 96.9\ \mu\text{rad}/\sqrt{\text{Hz}}$ up to 1 Hz due to star-tracker).

Performance: Recall that in the drag-free control formulation, the normalized thrust noise curve was scaled by a factor of two to account for the input disturbance term $\delta \boldsymbol{f}_{eq}$ in the drag-free equations of motion. This induces a performance bound for the closed-loop attitude dynamics that will guide the design of the attitude controller. Given that $\boldsymbol{r}_{eq} = [1.5 \cdot 10^{-2}, 0, 0]^T$ m, the disturbance term $\delta \boldsymbol{f}_{eq}$ is given by:

$$\delta \boldsymbol{f}_{eq} = -1.5\begin{bmatrix}0\\ 10^{-2}\dot{\omega}_z\\ -10^{-2}\dot{\omega}_y\end{bmatrix} - 1.5\begin{bmatrix}-10^{-2}\left(\omega_y^2+\omega_z^2\right)\\ 10^{-2}\omega_x\omega_y\\ 10^{-2}\omega_x\omega_z\end{bmatrix}.$$

Within the MGRS science band $\mathcal{B}$, the normalized thrust noise upper bound for each axis is less than $0.5 \cdot 10^{-8}\ \text{ms}^{-2}/\sqrt{\text{Hz}}$. Taking this as the upper bound for the noise floor due to $\delta \boldsymbol{f}_{eq}$ (hence the factor of two), and noting that $\omega_x \approx \bar{n} \approx 10^{-3}$ rad/s, we obtain the following approximate bounds:

$$\widetilde{\omega}_y(f), \widetilde{\omega}_z(f) < 0.1\ \mu\text{rad s}^{-2}/\sqrt{\text{Hz}},\ \widetilde{\omega}_y(f), \widetilde{\omega}_z(f) < 100\ \mu\text{rad s}^{-1}/\sqrt{\text{Hz}},\ f \in \mathcal{B}.$$

Using the linearized approximation for ω given in (24), we obtain the following performance bounds on the Euler angles and their time derivatives:

$$\begin{bmatrix}\widetilde{\phi}(f)\\ \widetilde{\psi}(f)\end{bmatrix} < \begin{bmatrix}10^{-1}\\ 10^{-1}\end{bmatrix}\text{rad}/\sqrt{\text{Hz}},\ \begin{bmatrix}\widetilde{\dot{\theta}}(f)\\ \widetilde{\dot{\phi}}(f)\\ \widetilde{\dot{\psi}}(f)\end{bmatrix} < \begin{bmatrix}100\\ 100\\ 100\end{bmatrix}\mu\text{rad s}^{-1}/\sqrt{\text{Hz}},\ \begin{bmatrix}\widetilde{\ddot{\phi}}(f)\\ \widetilde{\ddot{\psi}}(f)\end{bmatrix} < \begin{bmatrix}0.1\\ 0.1\end{bmatrix}\mu\text{rad s}^{-2}/\sqrt{\text{Hz}}, \tag{27}$$

for $f \in \mathcal{B}$. Note that an exact knowledge of $\boldsymbol{r}_{eq}$, which in turn requires knowledge of the center of mass of the satellite, is *not* needed to derive the performance bounds above. The control center may be defined with respect to the center of the DOSS cavity. However, as long as the center of mass of the satellite is close to the control center, i.e. if there exists some small $\delta > 0$ such that $\|\boldsymbol{r}_{eq}\|_2 < \delta$ we can use this bound to derive analogous performance constraints on the Euler angles and their rates.

To construct the attitude control loop, we define the following functions in analogous fashion to the drag-free control diagram: plant model G_a as derived from (25); attitude controller K_a; input disturbance

weight $W_{d_a} = \text{diag}(M_{d_x}, M_{d_y}, M_{d_z})$, where M_{d_i} is the net input disturbance weight for the i^{th} axis (Figure 10); noise weight W_{n_a}, diagonal matrix with constant noise $61.475\ \mu\text{rad}/\sqrt{\text{Hz}}$; FEEP first order response model (identical to the response for net force); delay $D_a = \text{diag}(d_a, d_a, d_a)$, where d_a is a first order Padé approximation for a delay of 300 ms (100 ms sampling delay due to control digitization at 5 Hz, and 200 ms for one sample period hold); diagonal performance weights $W_{p_a} = \text{diag}(w_{p_a}, w_{p_a}, w_{p_a})$, $W_{u_a} = \text{diag}(w_{u_a}, w_{u_a}, w_{u_a})$, and $W_{\dot{p}_a}$ defined as

$$W_{\dot{p}_a} = \begin{bmatrix} 0 & w_{\dot{p}_a} & 0 \\ 0 & 0 & w_{\dot{p}_a} \end{bmatrix},$$

with associated performance variables z_{e_a}, z_{u_a}, and $z_{\dot{e}_a}$ respectively. The control diagram is virtually identical to the one in Figure 7 and is omitted here for brevity. The main structural difference is the inclusion of the additional performance weight $W_{\dot{p}_a}$ which enforces the angular acceleration bounds given in (27). Note that by leveraging a more judicious choice for w_{p_a} and the acceleration weight function $w_{\dot{p}_a}$, we eliminated the requirement for an additional weighting function for the performance bounds on the angular rates. All three weighting functions w_{p_a}, $w_{\dot{p}_a}$, and w_{u_a} are plotted below in Figure 11 and discussed in the text thereafter.

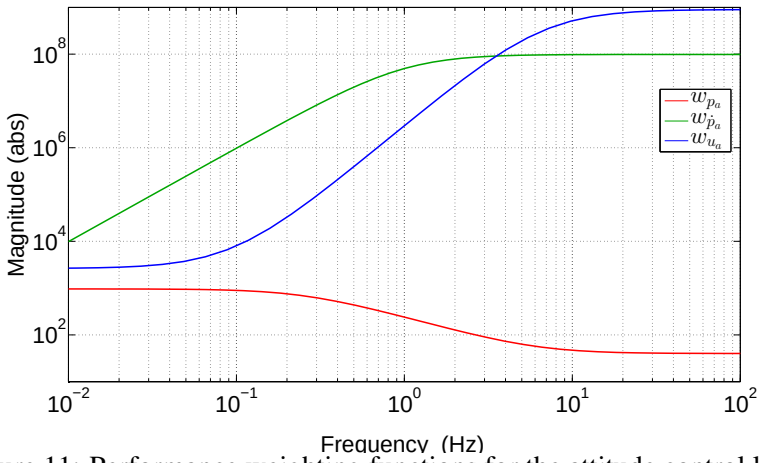

Figure 11: Performance weighting functions for the attitude control loop.

The closed-loop equation from the normalized disturbances and noise inputs to the performance variables z_{e_a}, $z_{\dot{e}_a}$ and z_{u_a} is given by:

$$\begin{bmatrix} z_{e_a} \\ z_{\dot{e}_a} \\ z_{u_a} \end{bmatrix} = \underbrace{\begin{bmatrix} W_{p_a} S_{o_a} G_a W_{d_a} & -W_{p_a} T_{o_a} W_{n_a} \\ W_{\dot{p}_a} S_{o_a} G_a W_{d_a} & -W_{\dot{p}_a} T_{o_a} W_{n_a} \\ -W_{u_a} S_{I_a} K_a G_a W_{d_a} & W_{u_a} S_{I_a} K_a W_{n_a} \end{bmatrix}}_{:=N_a} \begin{bmatrix} d_a \\ n_a \end{bmatrix}, \tag{28}$$

where $S_{o_a}, S_{I_a}, T_{o_a}$ are defined analagously to (22), using instead, the systems G_a, D_a and K_a. The performance bounds in (27) introduce certain constraints on achievable performance and are summarized below.

- The input disturbance rejection constraints for minimizing the Euler angles are quite benign in the sense that they impose lower bounds on the output sensitivity bandwidth to be greater than 3 mHz. The primary limitation arises from the effect of the input disturbances on the control signal. In particular, the transfer function from the input disturbances to the control torque u is given by $S_{I_a} K_a G_a$. At low frequencies, the singular values of this transfer function will be close to one, resulting in perfect transmission of the input disturbances to the control signal. For frequencies beyond about 0.01 Hz, this would lead to overly aggresive control.

- For the roll-yaw dynamics, the weighting function $w_{\dot{p}_a}$ for frequencies below 1 Hz is simply s^2 scaled by the inverse of the acceleration noise bound. For frequencies below the closed-loop bandwidth (i.e. where the singular values of T_{o_a} are approximately one), there is near perfect transmission from the noise to the output Euler angles. Given the noise value derived in (26), a closed-loop bandwidth (corresponding to the output complementary sensitivity) greater than 0.01 Hz would be infeasible with respect to the desired acceleration upper bounds given in (27). As a result, the performance requirements on the angular acceleration are relaxed to 0.4 μrad $\mathrm{s}^{-2}/\sqrt{\mathrm{Hz}}$ in an attempt to alleviate the bandwidth restrictions.

The results of the $H_\infty-$optimization, conducted separately for the roll-yaw and pitch systems are summarized in Figure 12.

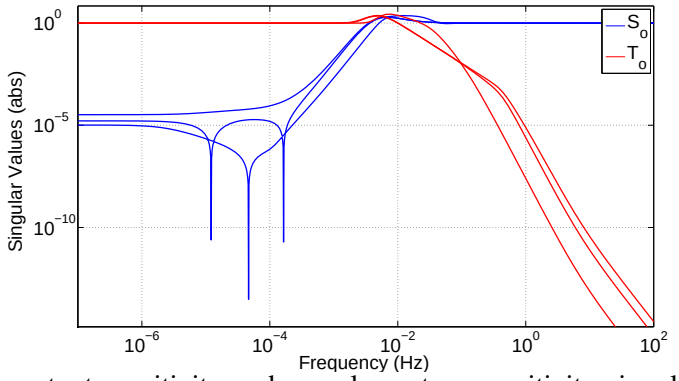

Figure 12: Closed-loop output sensitivity and complementary sensitivity singular values for the attitude dynamics.

In addition to the $H_\infty-$norm for N, we also consider the singular values of the following system:

$$N_{\dot{a}} := \mathrm{diag}(s,s,s)\begin{bmatrix} S_{o_a}G_aW_{d_a} & -T_{o_a}W_{n_a}\end{bmatrix},$$

which represents the closed-loop transfer function from the normalized disturbances and noise to the Euler angular rate ASDs. The closed-loop sensitivity bandwidth is 5.14 mHz for pitch and 3.51 mHz for the roll/yaw system (close to the predicted lower bound of 3 mHz), while the complementary sensitivity bandwidth (defined by the frequency at which $\bar{\sigma}(T_o)$ crosses $1/\sqrt{2}$ from above) is 0.0283 Hz for pitch and 0.012 Hz for the roll/yaw system, courtesy of relaxing the angular acceleration performance bounds. The $H_\infty-$norms for N and $N_{\dot{a}}$ were calculated to be $0.6493 < 1$, and $9.53 \cdot 10^{-6}$ respectively, which confirms that the angular rate bounds are also satisfied. We are now ready to test our controllers in the full non-linear setting.

7. Simulation Results

In this section we present simulation results from implementing the controllers formulated in the previous section within the high-fidelity simulation environment discussed in Section 5. The controllers are first digitized (at 10 Hz for drag-free and 5 Hz for attitude) using the Tustin method and augmented with one sample period delay. All noise sources were simulated by shaping white noise with unity spectral density by a low-pass filter and a shaping filter that approximates the expected bound on the noise source (see for example, Figures 4 and 5). We assume a constant propellant mass flow rate given by the following expression:

$$\dot{m}_s = -8\frac{\bar{F}}{g_0\bar{I}_{sp}},$$

where $\bar{F} = 30$ μN is the average assumed thrust from 8 thrusters, $\bar{I}_{sp} = 4000$ s is an estimate of the average specific impulse, and $g_0 = 9.81$ ms^{-2}. This yields an average flow rate of about 0.022 g/hr. The propellant is expelled evenly from the three cluster assemblies. This ensures that the center of mass of the satellite with respect to the geometric center is fixed within the body frame, and therefore maintains consistency with our earlier assumption of treating the vector $\boldsymbol{r}_{eq}$, a design variable, fixed with respect to the center of mass. The time varying density is used to update the inertial properties of the satellite and the gravity gradient calculations. Finally, in order to curb simulation time, the linear programming algorithm for thrust allocation was tested a posteriori (see Appendix 11.2.).

Figures 13a and 13b show the drag-free control error $\boldsymbol{r}_c$ (resolved in the satellite body frame) and Euler angles (θ, ϕ, ψ) respectively. After an initial overshoot (< 225 nm in the $x-$axis), the test mass stays within 50 nm of the equilibrium point in the $x-$axis, and ± 30 nm in the y and z axes. Similarly, after an initial overshoot ($< 0.007^o$ in yaw), the pitch angle stays within $\pm 0.004^o$, and the roll and yaw angles stay within $\pm 0.006^o$.

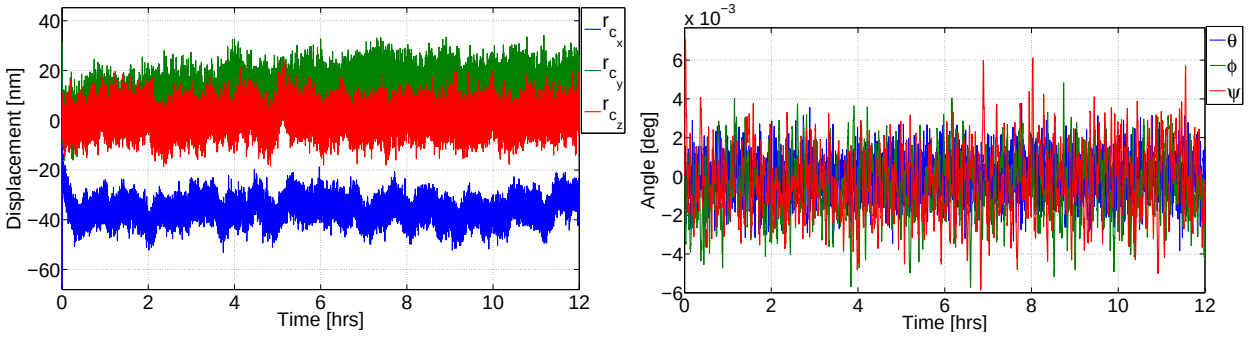

(a) Drag-free control error $\boldsymbol{r}_c$. (b) Euler angles (θ, ϕ, ψ).

Figure 13: Translational and Attitude control accuracy. At steady state, $\boldsymbol{r}_c$ remains within 50 nm in x and ± 30 nm in y and z axes, and pitch, roll and yaw angles stay within $\pm[0.004^o, 0.006^o, 0.006^o]$.

Figures 14a and 14b show the commanded force and torques from the drag-free and attitude controllers quantized in steps of 0.1 μN and 0.1 μNm respectively. Note that all commanded forces and torques are within the envelope predicted in Section 5.4. To test the thruster allocation algorithm, the optimization objective in Problem $\mathcal{OPT}$ (see Appendix 11.2.) was augmented by adding a term equal to the l^1 norm of the difference between the current and previous thrust allocation solution. This was done to avoid large step changes in the individual thrust commands between sampling intervals. On average, all thrusters operated below 10 μN, peak thrust across all thrusters was less than 28 μN, and the average solve time for the optimization algorithm was on the order of 0.1 ms, which is well below the 100 ms delay margin.

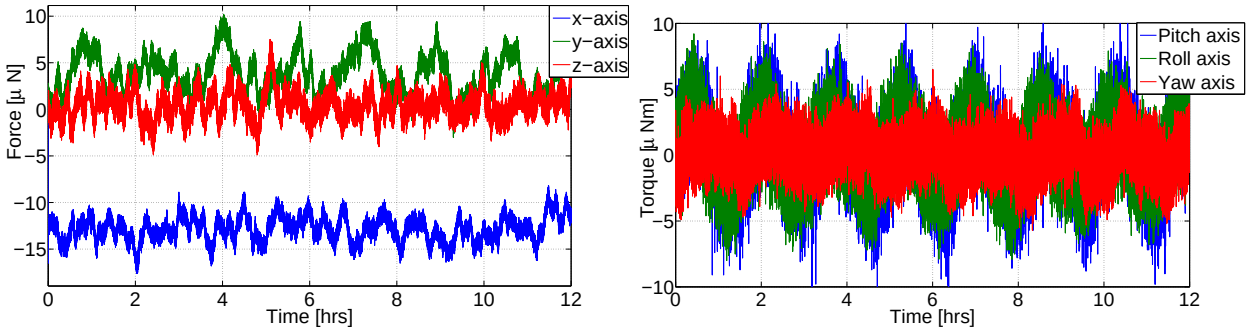

(a) Net commanded force from drag-free controller. (b) Net commanded torque from attitude controller.

Figure 14: Net command force and torque.

Finally, the ASD of the residual inertial acceleration of the proof mass given by the sum of $\boldsymbol{f}_{dp}$ and $\boldsymbol{f}_{sp}$ is presented in Figure 15. The noise curves were obtained by implementing Welch's spectral density estimation algorithm using three 4-hour segments with 50% overlap and a Hamming window [59].

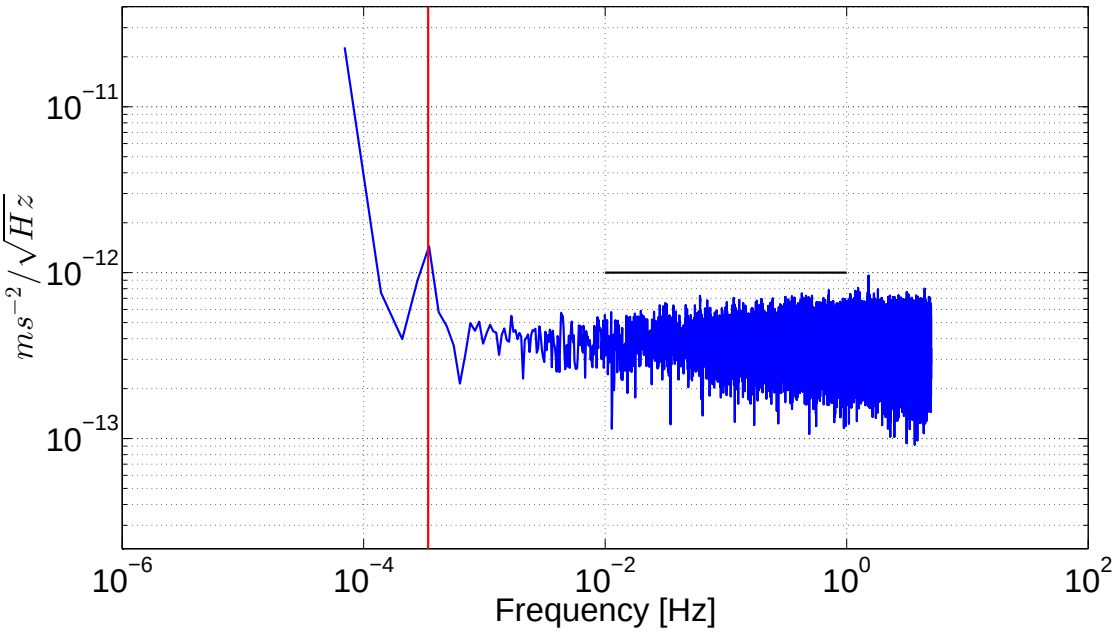

Figure 15: Residual acceleration ASD along inertial X axis (Bias removed). The red line indicates the second harmonic of the mean orbital frequency (≈ 0.342 mHz), and the black line indicates the performance upper bound. The other two axes are very similar.

Figure 15 shows that the satellite achieves its target drag-free performance specification with a measurable margin for error under "nominal" conditions. By "nominal" we specifically refer to the unity DC gain assumption for the FEEP time response, and knowledge of the mass distribution which allows us to calculate $\boldsymbol{r}_{eq}$ and bound $\delta\boldsymbol{f}_{eq}$ exactly. In future work, these assumptions will be relaxed and explicit plant uncertainty sets for the drag-free and attitude dynamics will be constructed within a robust control design framework.

8. Conclusions

In this paper we first presented modeling assumptions and the development of a high-fidelity simulation environment for the MGRS mission. Next, we used the envelope of expected disturbances computed by the simulator to select a suitable micropropulsion system, subject to the mass, volume and power limitations of the MGRS microsatellite bus. Finally, we designed drag-free and attitude controllers using "nominal" parameters (e.g. expected spin rate and satellite inertial properties) by employing tools from $H_\infty-$optimization. The controllers were discretized and implemented with delays within the full nonlinear simulation environment and the resulting non-gravitational accelerations on the test mass were verified to be under 10^{-12} ms$^{-2}/\sqrt{\text{Hz}}$ within the MGRS science frequency band $\mathcal{B}$. These results lend credence to the possiblity of using microsatellites for conducting precise gravitational and relativistic science at a fraction of the cost of most monolithic missions.

The robustness properties of the drag-free controller were discussed only in passing by conducting a Monte Carlo simulation with respect to the uncertain parameters within the plant dynamics. In future work, we will investigate the robust stability and performance characteristics of the drag-free and attitude controllers in much more detail. In addition, we will also develop a full EKF for estimating the satellite attitude states and

net disturbance forces and torques on the satellite which will enable aeronomic and geodetic data return.

9. Acknowledgements

We would like to thank Dr. Walter Fichter at The University of Stuttgart for his valuable feedback on the drag-free control design. We also thank Christian Altmann and Hans Leiter at Airbus Defense and Space for their calculations and feedback on the Giessen μN ion engines. This work was supported in part by the Stanford Graduate Fellowship (SGF) and the King Abdulaziz City for Science and Technology (KACST).

10. References

[1] Lange, B. "The Drag-Free Satellite." AIAA Journal, Vol. 2, No. 9, pp. 1590–1606, Sep. 1964. ISSN 0001-1452. doi:10.2514/3.55086.

[2] Leitner, J. "Investigation of Drag-Free Control Technology for Earth Science Constellation Missions." Tech. rep., Final Study Report to NASA Earth Science Technology Office, 2003.

[3] Rodrigues, M. and Touboul, P. "The LISA accelerometer." Advances in Space Research, Vol. 32, No. 7, pp. 1251–1254, 2003.

[4] Sun, K.-X., Allen, G., Buchman, S., DeBra, D., and Byer, R. "Advanced Gravitational Reference Sensor for High Precision Space Interferometers." Classical and Quantum Gravity, Vol. 22, No. 10, p. S287, 2005.

[5] DeBra, D. "Drag-Free Control for Fundamental Physics Missions." Advances in Space Research, Vol. 32, No. 7, pp. 1221–1226, 2003.

[6] Laboratory, J. H. A. P., Guidance, S., and Laboratory, C. "A Satellite Freed of all but Gravitational Forces:" TRIAD I"." Journal of Spacecraft and Rockets, Vol. 11, No. 9, pp. 637–644, 1974.

[7] Everitt, C., DeBra, D., Parkinson, B., Turneaure, J., Conklin, J., Heifetz, M., Keiser, G., Silbergleit, A., Holmes, T., Kolodziejczak, J., et al. "Gravity Probe B: Final Results of a Space Experiment to Test General Relativity." Physical Review Letters, Vol. 106, No. 22, p. 221101, 2011.

[8] Cesare, S., Aguirre, M., Allasio, A., Leone, B., Massotti, L., Muzi, D., and Silvestrin, P. "The Measurement of Earth's Gravity Field after the GOCE Mission." Acta Astronautica, Vol. 67, No. 7, pp. 702–712, 2010.

[9] Li, J., Bencze, W., DeBra, D., Hanuschak, G., Holmes, T., Keiser, G., Mester, J., Shestople, P., and Small, H. "On-orbit Performance of Gravity Probe B Drag-Free Translation Control and Orbit Determination." Advances in Space Research, Vol. 40, No. 1, pp. 1–10, 2007.

[10] McNamara, P., Vitale, S., Danzmann, K., and LISA Pathfinder Science Working Team and others. "LISA Pathfinder." Classical and Quantum Gravity, Vol. 25, No. 11, p. 114034, 2008.

[11] Reitze, D., González, G., Mather, J., and Stebbins, R. "Gravitational Waves." Scientific American, Vol. 310, No. 2, pp. 6–6, 2014.

[12] Berg, J., Touboul, P., and Rodrigues, M. "Status of MICROSCOPE, A Mission to Test the Equivalence Principle in Space." Journal of Physics: Conference Series, Vol. 610, No. 1, 2015.

[13] Sun, K.-X., Allen, G., Buchman, S., Byer, R. L., Conklin, J. W., DeBra, D. B., Gill, D., Goh, A., Higuchi, S., Lu, P., et al. "Progress in Developing the Modular Gravitational Reference Sensor." "Laser Interferometer Space Antenna: 6th International LISA Symposium," Vol. 873, pp. 515–521. AIP Publishing, 2006.

[14] Zoellner, A., Hultgren, E., and Sun, K.-X. "Integrated Differential Optical Shadow Sensor for Modular Gravitational Reference Sensor.", 2013.

[15] Ardaens, J., D'Amico, S., and Montenbruck, O. "Final Commissioning of the PRISMA GPS Navigation System." Journal of Aerospace Engineering, Vol. 4, No. 3, p. 105, 2012.

[16] Montenbruck, O. and DAmico, S. "GPS Based Relative Navigation." "Distributed Space Missions for Earth System Monitoring," pp. 185–223. Springer, 2013.

[17] D'Amico, S., Pavone, M., Saraf, S., Alhussien, A., Al-Saud, T., Buchman, S., Byer, R., and Farhat, C. "Miniaturized Autonomous Distributed Space System for Future Science and Exploration." "Int. Workshop on Satellite Constellations and Formation Flying," Delft, Netherlands, Jun. 2015.

[18] Baker, D. N. and Worden, S. P. "The Large Benefits of Small-Satellite Missions." EOS, Transactions American Geophysical Union, Vol. 89, No. 33, pp. 301–302, 2008.

[19] Nguyen, A. and Conklin, J. "Three-Axis Drag-Free Control and Drag Force Recovery of a Single-Thruster Small Satellite." AIAA Journal of Spacecraft and Rockets, pp. 1–11, 2015.

[20] Bencze, W., DeBra, D., Herman, L., Holmes, T., Adams, M., Keiser, G., and Everitt, C. "On-orbit Performance of the Gravity Probe B Drag-Free Translation Control System." "29th AAS GN&C Conference," Breckenridge, Colorado, 2006.

[21] Canuto, E., Molano, A., and Massotti, L. "Drag-Free Control of the GOCE Satellite: Noise and Observer Design." IEEE Transactions on Automatic Control, Vol. 18, No. 2, pp. 501–509, 2010.

[22] Noci, G., Matticari, G., Siciliano, P., Fallerini, L., Boschini, L., and Vettorello, V. "Cold Gas Micro Propulsion System for Scientific Satellites fine pointing: Review of Development and Qualification activities at Thales Alenia Space Italia." "45th AIAA/ASME/SAE/ASEE Joint Propulsion Conference and Exhibit," Denver, Colorado, 2009.

[23] Vallado, D., Seago, J., and Seidelmann, P. "Implementation Issues Surrounding the New IAU Reference Systems for Astrodynamics." "AAS Astrodynamics Specialist Conference," pp. 06–134. AIAA, Tampa, Florida, Jan. 2006.

[24] Gerardi, D., Allen, G., Conklin, J. W., Sun, K., DeBra, D., Buchman, S., Gath, P., Fichter, W., Byer, R. L., and Johann, U. "Invited Article: Advanced Drag-Free Concepts for Future Space-based Interferometers: Acceleration Noise Performance." Review of Scientific Instruments, Vol. 85, No. 1, 2014.

[25] Cunningham, L. "On the Computation of the Spherical Harmonic Terms Needed During the Numerical Integration of the Orbital Motion of an Artificial Satellite." Celestial Mechanics, Vol. 2, No. 2, pp. 207–216, 1970.

[26] McCarthy, D. and Petit, G. "IERS conventions (2003)." Tech. rep., DTIC Document, 2004.

[27] Schaub, H. and Junkins, J. Analytical Mechanics of Space Systems. AIAA Education Series, Reston, VA, 2nd edn., October 2003. doi:10.2514/4.861550.

[28] Montenbruck, O. and Gill, E. Satellite Orbits: Models, Methods and Applications. Springer Science & Business Media, 2012.

[29] Graziano, B. Computational Modelling of Aerodynamic Disturbances on Spacecraft Within a Concurrent Engineering Framework. Ph.D. thesis, Cranfield University, 2007.

[30] Hedin, A., Fleming, E., Manson, A., Schmidlin, F., Avery, S., Clark, R., Franke, S., Fraser, G., Tsuda, T., Vial, F., and Vincent, R. "Empirical Wind Model for the Upper, Middle and Lower Atmosphere." Journal of Atmospheric and Terrestrial Physics, Vol. 58, No. 13, pp. 1421 – 1447, 1996. ISSN 0021-9169. doi:http://dx.doi.org/10.1016/0021-9169(95)00122-0.

[31] Schaaf, S. and Chambré, P. Flow of Rarefied Gases. Princeton University Press, 1961.

[32] Schatten, K. "Fair Space Weather for Solar Cycle 24." Geophysical Research Letters, Vol. 32, No. 21, 2005.

[33] Suggs, R., Euler, H., and Smith, S. "Future Solar Activity Estimates for use in Prediction of Space Environmental Effects on Spacecraft Orbital Lifetime and Performance." Tech. rep., NASA, Marshall Space Flight Center. http://sail. msfc. nasa. gov/current_solar_report/CurRpt. pdf. File dated November, 2011.

[34] McCarthy, D. "IERS Conventions (1996)." IERS Technical Note, Vol. 21, pp. 1–95, 1996.

[35] Bettadpur, S. "GRACE Product Specification Document." Center for Space Research, The University of Texas at Austin, 2007.

[36] Knocke, P., Ries, J., and Tapley, B. "Earth Radiation Pressure Effects on Satellites." "AAS Astrodynamics Specialist Conference," pp. 577–586. Minneapolis, Minnesota, Aug. 1988.

[37] Allman, G. "On the Attraction of Ellipsoids, with a New Demonstration of Clairaut's Theorem, Being an Account of the Late Professor Mac Cullagh's Lectures on Those Subjects." The Transactions of the Royal Irish Academy, pp. 379–395, 1849.

[38] Swank, A. Gravitational Mass Attraction Measurement for Drag-Free References. Ph.D. thesis, Stanford University - Aeronautics and Astronautics, May 2009.

[39] Jarrige, J., Thobois, P., Blanchard, C., Elias, P.-Q., Packan, D., Fallerini, L., and Noci, G. "Thrust Measurements of the GAIA Mission Flight-Model cold gas thrusters." Journal of Propulsion and Power, Vol. 30, No. 4, pp. 934–943, 2014.

[40] Hans, J., Altmann, C., Kukies, R., and Lauer, D. "Miniaturizing Radio-Frequency Ion Thrusters and Systems – Technology Development and Applications." "50th AIAA/ASME/SAE/ASEE Joint Propulsion Conference," AIAA Paper 2014-3911. Cleveland, Ohio, 2014.

[41] Hruby, V., Gamero-Castano, M., Spence, D., Gasdaska, C., Demmons, N., McCormick, R., Falkos, P., Young, J., and Connolly, W. "Colloid thrusters for the new millennium, ST7 DRS mission." "IEEE Aerospace Conference," Vol. 1. IEEE, 2004.

[42] Paita, L., Ceccanti, F., Spurio, M., Cesari, U., Priami, L., Nania, F., Rossodivita, A., and Andrenucci, M. "Alta's FT-150 FEEP microthruster: development and qualification status." "Proceeding of the 31st International Electric Propulsion Conference, IEPC-09-186," Ann Arbor, Michigan, 2009.

[43] Paita, L., Cesari, U., Nania, F., Priami, L., Rossodivita, A., Giusti, N., Andrenucci, M., and Estublier, D. "Alta FT-150: The Thruster for LISA Pathfinder and LISA/NGO Missions." "9th LISA Symposium," Vol. 467 of *Astronomical Society of the Pacific Conference Series*, pp. 245–249. Paris, 2013.

[44] Wright, W. and Ferrer, P. "Electric micropropulsion systems." Progress in Aerospace Sciences, Vol. 74, pp. 48–61, 2015.

[45] Altmann, C. and Leiter, H. Personal communication, Aug. 2015.

[46] Nicolini, D., Frigot, P.-E., Musso, F., Cesare, S., Castorina, G., Ceruti, L., Bartola, F., Zanella, P., Ceccanti, F., Priami, L., et al. "Direct Thrust and Thrust Noise Measurements on the LISA Pathfinder Field Emission Thruster." "31st International Electric Propulsion Conference, IEPC-2009-183," Ann Arbor, MI, 2009.

[47] Tinto, M., DeBra, D., Buchman, S., and Tilley, S. "gLISA: geosynchronous laser interferometer space antenna concepts with off-the-shelf satellites." Review of Scientific Instruments, Vol. 86, No. 1, p. 014501, 2015.

[48] Ziegler, T. and Fichter, W. "Test Mass Stiffness Estimation for the LISA Pathfinder Drag-Free System." "AIAA Conf. on Guidance, Navigation and Control," Vol. 6669. Hilton Head, South Carolina, Aug. 2007.

[49] Zoellner, A., Alfauwas, A., Buchman, S., Byer, R., Cutler, G., DeBra, D., Eddy, D., Lipa, J., Lui, C., Saraf, S., and Singh, S. "Drag-Free Technology on a Small Satellite." "Int. Astronautical Congress," 2015. To appear.

[50] Fichter, W., Gath, P., Vitale, S., and Bortoluzzi, D. "LISA Pathfinder Drag-Free Control and System Implications." Classical and Quantum Gravity, Vol. 22, No. 10, p. S139, 2005.

[51] Fichter, W., Schleicher, A., Bennani, S., and Wu, S. "Closed Loop Performance and Limitations of the LISA Pathfinder Drag-Free Control System." "AIAA Conf. on Guidance, Navigation and Control," pp. 20–3. Hilton Head, South Carolina, 2007.

[52] Gath, P. F., Fichter, W., Kersten, M., and Schleicher, A. "Drag free and attitude control system design for the LISA pathfinder mission." "AIAA Conf. on Guidance, Navigation and Control," Vol. 5430. Providence, Rhode Island, Aug. 2004.

[53] Pettazzi, L., Lanzon, A., Theil, S., and Finzi, A. E. "Design of Robust Drag-Free Controllers with Given Structure." AIAA Journal of Guidance, Control, and Dynamics, Vol. 32, No. 5, pp. 1609–1621, 2009.

[54] Pettazzi, L. and Lanzon, A. "Simultaneous optimization of performance weights and a controller in mixed-μ synthesis." Automatica, Vol. 48, No. 1, pp. 115–120, 2012.

[55] Skogestad, S. and Postlethwaite, I. Multivariable feedback control: analysis and design, Vol. 2. Wiley New York, 2007.

[56] Packard, A. What's New With μ: Structured Uncertainty in Multivariable Control. Ph.D. thesis, University of California, Berkeley, 1988.

[57] Chesi, G., Garulli, A., Tesi, A., and Vicino, A. "Homogeneous Lyapunov Functions for Systems with Structured Uncertainties." Automatica, Vol. 39, No. 6, pp. 1027–1035, 2003.

[58] Poola, K. and Tikku, A. "Robust performance against time-varying structured perturbations." IEEE Transactions on Automatic Control, Vol. 40, No. 9, pp. 1589–1602, 1995.

[59] Tröbs, M. and Heinzel, G. "Improved spectrum estimation from digitized time series on a logarithmic frequency axis." Measurement, Vol. 39, No. 2, pp. 120–129, 2006.

11. Appendix

11.1. Satellite Drawings

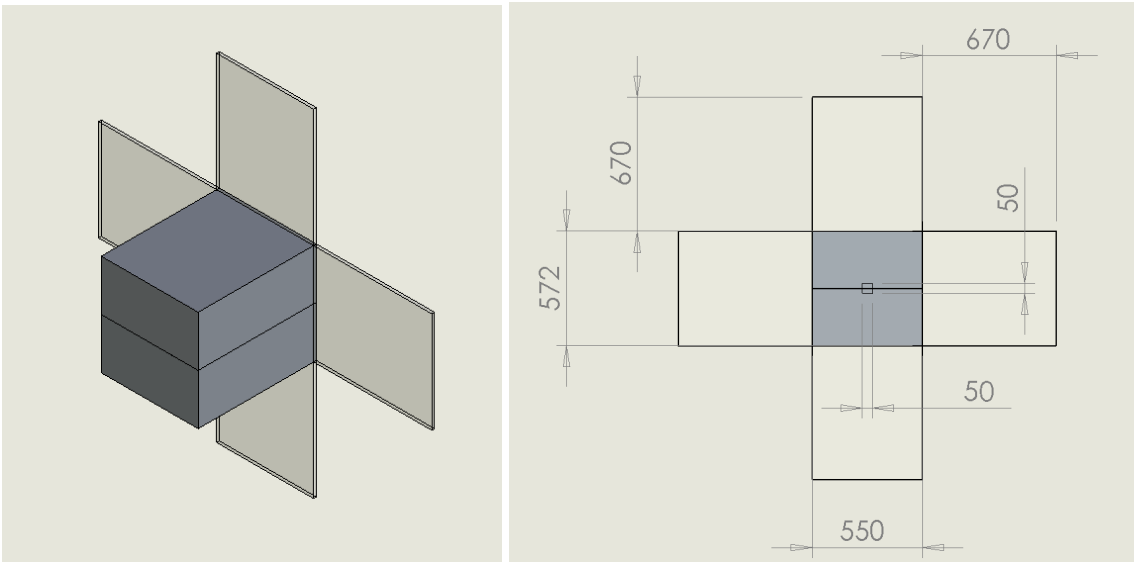

(a) Isometric view.

(b) Front view.

(c) Top view.

Figure 16: Satellite external and DOSS cavity internal dimensions (in mm).

11.2. Thruster Configuration Design

Let $\boldsymbol{T} \in \mathbb{R}^n$ be a vector representing the thrust levels for all n thrusters on board the spacecraft, and let $\tilde{\boldsymbol{F}} := [\boldsymbol{F}_c^T, \boldsymbol{M}_c^T]^T$ denote the commanded force and torque vector as dictated by the drag-free and attitude control algorithms. Define $A \in \mathbb{R}^{6\times n}$ to be the configuration matrix such that the achieved force and torque for a given set of positive thrusts $\boldsymbol{T}$ is given by:

$$\begin{bmatrix} \boldsymbol{F}_c \\ \boldsymbol{M}_c \end{bmatrix} = A\boldsymbol{T}.$$

The design objective then is to find a placement and orientation for a set of thrusters (i.e. find A) such that the arrangement can produce all required force and torques as determined by the disturbance simulations discussed in the main body of the paper, while respecting the lower and upper bound constraints on the

thrust for each thruster. Given the disturbance calculations, we define $\mathcal{F}$ to be the following polytope:

$$\begin{bmatrix} -30 \\ -20 \\ -10 \\ -10 \\ -10 \\ -10 \end{bmatrix} \preceq \tilde{\boldsymbol{F}} \preceq \begin{bmatrix} 10 \\ 20 \\ 10 \\ 10 \\ 10 \\ 10 \end{bmatrix},$$

where the forces are in μN, torques are in μNm, and $\preceq$ denotes component-wise inequality.

Let $V^{\mathcal{F}}$ be the $2^6 - 1$ vertices of the polytope $\mathcal{F}$. Then, for a given configuration matrix A, we define the following convex optimization problem:

Thruster Allocation, $\mathcal{OPT}$ — For all $\tilde{\boldsymbol{F}} \in V^{\mathcal{F}}$, solve

$$\begin{aligned} \min_{\boldsymbol{T} \in \mathbb{R}^n} \quad & \|\boldsymbol{T}\|_1 \\ \text{such that} \quad & A\boldsymbol{T} = \tilde{\boldsymbol{F}} \\ & \boldsymbol{T} \succeq \mathbf{1}_n \\ & \boldsymbol{T} \preceq T_{max}\mathbf{1}_n \end{aligned}$$

where $\mathbf{1}_n$ is a vector of 1s and T_{max} is the desired maximum thrust per thruster (constrained to be $< 100\mu$N). If the above problem is feasible for all $\tilde{\boldsymbol{F}} \in V^{\mathcal{F}}$, then A is a feasible configuration matrix. That is, for any $\tilde{\boldsymbol{F}} \in \mathcal{F}$, there exists a feasible $\boldsymbol{T}$ that can achieve the desired force and torque specified by $\tilde{\boldsymbol{F}}$. The search for (A, T_{max}) itself is non-convex and infinite-dimensional. By manually enumerating various configurations, we selected an arrangement with 9 thrusters grouped in 3 clusters of 3, with $T_{max} = 55\mu$N. This configuration is shown in Figure 17. Note that the feasibiliy problem is independent of the optimization objective in problem $\mathcal{OPT}$. In this scenario, we chose to minimize the 1-norm of $\boldsymbol{T}$ to minimize both fuel-rate and power consumption.

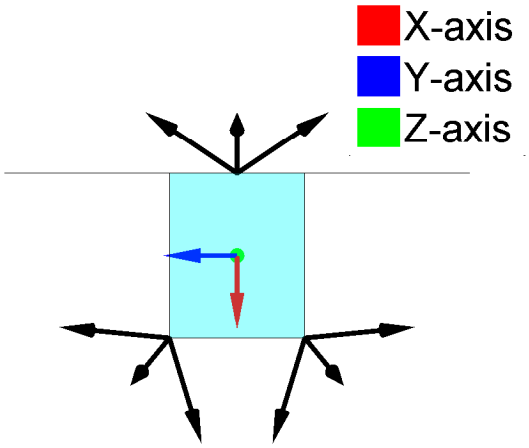

(a) Top View.

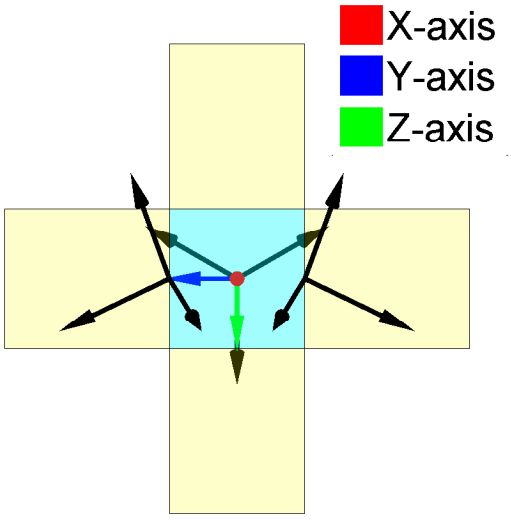

(b) Front view.

Figure 17: Thruster configuration for MGRS. Arrows indicate thruster plume directions.